Journal of Engineering for Gas Turbines and Power. Received July 29, 2018;
Accepted manuscript posted August 27, 2018. doi:10.1115/1.4041282

Gas Turbine Fouling Tests: Review, Critical Analysis and Particle Impact Behavior Map

Alessio Suman[1], Nicola Casari[1], Elettra Fabbri[1], Michele Pinelli[1], Luca di Mare[2], Francesco Montomoli[3]

[1] Dipartimento di Ingegneria, Università degli Studi di Ferrara, 44122 Ferrara, Italy

[2] St John's College, University of Oxford, St Giles, Oxford, OX1 3JP, United Kingdom

[3] Imperial College London, London, SW7 2AZ, United Kingdom

ABSTRACT

Fouling affects gas turbine operation and airborne or fuel contaminants, under certain conditions, become very likely to adhere to surfaces if impact takes place. Particle sticking implies the change in shape in terms of roughness of the impinged surface. The consequences of these deposits could be dramatic: these effects can shut an aircraft engine down or derate a land-based power unit. This occurrence may happen due to the reduction of the compressor flow rate and the turbine capacity, caused by a variation in the HPT nozzle throat area (geometric blockage due to the thickness of the deposited layer and the aerodynamic blockage due to the increased roughness, and in turn boundary layer).

Several methods to quantify particle sticking have been proposed in literature so far, and the experimental data used for their validation vary in a wide range of materials and conditions. The experimental analyses have been supported by (and have given inspiration to) increasingly realistic mathematical models. Experimental tests have been carried out on (i) a full scale gas turbine unit, (ii) wind tunnel testing or hot gas facilities using stationary cascades, able to reproduce the same conditions of gas turbine nozzle operation and finally, (iii) wind tunnel testing or hot gas facilities using a coupon as the target.

In this review, the whole variety of experimental tests performed is gathered and classified according to composition, size, temperature and particle impact velocity. Using particle viscosity and sticking prediction models, over seventy (70) tests are compared with each other and with the model previsions providing a useful starting point for a comprehensive critical analysis. Due to the variety of test conditions, the related results are difficult to be pieced together due to differences in particle material and properties.

The historical data of particle deposition obtained over thirty (30) years are classified using particle kinetic energy and the ratio between particle temperature and its softening temperature. Qualitative thresholds for the distinction between particle deposition, surface erosion and particle break-up, based on particle properties and impact conditions, are identified. The outcome of this paper can be used for further development of sticking models or as a starting point for new insight into the problem.

INTRODUCTION

Air and/or fuel contaminants can severely damage gas turbines in terms of erosion, for blades and annulus, and build-up of deposits on the airfoils. For land-based power units, filtration systems tend to limit the particles entering the machinery, but they are unable to completely prevent their ingestion [1]. Moreover, the depletion of natural gas resources results in the increase of alternative types of fuel for gas turbines. Such fuels always contain traces of ash and other contaminants that may be deposited on hot section surfaces, especially in the first stage, due to the higher temperature values.

In the case of jet engines, the main issues can be referred to compressor erosion and hot section fouling [2]. In particular, if the fouling of gas turbines results in performance degradation, the ingestion of sands or coal ashes can dramatically affect the machine efficiency. On the other hand, the erosion phenomena determine changes in compressor blade geometry that consequently cause modifications in jet engine performance. For these reasons, several efforts are focused on preventing engine failure, especially related to the encounters of jet engines with volcanic ashes [3, 4].

According to literature [5], there are four principal groups of particles that can be somehow related to gas turbine operation: ash, coal, bituminous coal and lignite. These contaminants are usually known as silica-based materials, characterized by atom-networks of silica.

Ash is the term that defines the pyroclastic particles with a diameter less than 2 mm, ejected from volcanos without considering shape or composition. Coal is the carbon-rich mineral material formed from the deposit of fossil plants. By the coalification process, different ranks of coal are produced as peat, bituminous coals, lignite and anthracite that are characterized by different percentages of volatile elements, moisture and carbon.

These first definitions give the opportunity to distinguish *a priori* the numerous experimental tests reported in literature related to particle deposition in hot gas turbine sections. These tests usually involve semi-molten particles; such a characteristic implies several difficulties in the description of the thermophysical properties. At the same time, the variation of the type of contaminant in terms of chemical composition combined with different test conditions (such as temperature and velocity) makes it more difficult to comprise the particle sticking mechanisms.

Early experimental analyses are related to deposits caused by fuel contamination without specific details about particle sticking capability [6 – 16]. In order to gain some insight into the sticking mechanism, one of the first analyses reported in literature starts investigating the influence of particle temperature variation for each composite [17]. This was firstly accomplished using a specific facility, with a full scale aero engine, that reproduced realistic environmental conditions of particle-laden clouds in order to evaluate the extent of the deterioration [18 – 20] in the case of volcanic ash ingestion. More recently, Shinozaki *et al.* [21] use a micro gas turbine

(Pegasus HP®) for studying volcanic ash adhesion by means of borescope internal analysis. Despite the very detailed information related to the performance deterioration due to particle ingestion, in recent years, these full-scale test facilities have been replaced by simplified stationary test-rigs in which the particle impact conditions can be easily controlled and measured representing the basis for drawing particle sticking/bouncing models. Accelerated deposition tests, able to recreate actual gas turbine conditions (air flow temperature and velocity), are carried out in order to study specific cause-effect relations on particle sticking mechanisms using simplified targets [22 – 40] or using a gas turbine nozzle [42 – 49]. Moreover, particular attention is drawn to cooling hole clogging that is considered the most detrimental phenomenon in gas turbine hot sections, especially for aero-engines [50 – 53] for which the performance and the reliability of the blade cooling system represents the most important aspect [54]. Besides particle adhesion, particle impact could determine surface erosion [55 – 57] or particle splashing [37]. As reported in the references, test conditions determine (i) the capability of the particle to remove surface materials or (ii) particle breaking.

Each experimental test is characterized by specific particle properties (material, dimension, etc.), airflow conditions (velocity, temperature, etc.) and target shapes and dimensions. For these reasons, the quantitative comparison between two or more tests is difficult to perform.

Aim of the paper. This work collects over seventy (70) particle deposition tests reported in literature, conducted using similar conditions and materials involved in particle deposition on hot gas turbine sections. For each of the performed tests, particle characteristics (size, composition, density), gas conditions (velocity, temperature) and target typology and dimensions are collected, grouped and post-processed in order to generate a useful map representing all of the possible consequences of a particle impact. In detail, this paper includes the following points:

- collection and comparison of the literature experimental tests related to gas turbine fouling;
- application of the most used particle sticking models for gas turbine particle adhesion, highlighting how each model works and where it fails if compared with the actual test results. Specific models for predicting particle characteristics such as viscosity and softening temperature are used and compared;
- creation of a map intended to be a prediction tool in relation with the particle deposition and erosion phenomena.

PARTICLE STICKING MODELS

The contaminants could stick to blade surfaces according to the material of the interacting bodies, the surface conditions, the particle size, the impact velocity and the impact angle. Sticking mechanisms could be affected by the presence of third substances or second phases (for semi-molten or molten particles) at the particle/surface interface [58, 59]. Particle adhesion, in hot gas turbine sections, is determined by the presence of a molten phase on the blade surfaces or the particle itself must be in a semi-molten state. Therefore, the

Journal of Engineering for Gas Turbines and Power. Received July 29, 2018;
Accepted manuscript posted August 27, 2018. doi:10.1115/1.4041282

characteristics that strongly affect the sticking probability are particle temperature, viscosity, surface tension and wettability [60, 61]. Unfortunately, silica-based materials are not pure substances, showing temperature-dependent variation of their physical characteristics.

Starting from these considerations, different sticking models used for hot particle deposition and more specifically for gas turbine particle adhesion have been developed over the years. Among others, in this work two models based on two different criteria are considered. These models will be useful for the subsequent data post-process.

Given the several different experimental tests collected in this review, only the basic formulation of the sticking models is considered. However, for the sake of completeness, for each sticking model a detailed description of the most recent upgrades is also reported. New formulations are characterized by model coefficients based on specific experimental tests that determine the impossibility to extend their validity to past tests for which no detailed information is usually available.

Critical viscosity model. This model correlates particle viscosity to a reference viscosity at which sticking starts. When particle viscosity μ is less than or equal to the critical value μ_c, the sticking probability value is assumed equal to 1 (one), whereas for higher particle viscosity (and in turn lower temperature), the particle sticking probability is calculated according to the relation

$$P_{\text{visc}} = \mu_c/\mu \;\; ; \;\; \mu_c = \mu_{\text{soft}} \tag{1}$$

where P_{visc} is the sticking probability related to the viscosity effect and μ_{soft} is the particle viscosity at the softening temperature while μ is the viscosity of the particle at its temperature. Therefore

$$P_{\text{visc}} = \begin{cases} \mu_c/\mu & \mu > \mu_c \\ 1 & \mu \leq \mu_c \end{cases} \tag{2}$$

This basic formulation highlights how the probability of sticking should be dependent on the particle viscosity in relation with the reference value μ_c considered as the threshold for ideal adhesion. Developments of this models were reported in literature regarding the transition across the critical viscosity value [62], the extension of the model validity to lower temperature [63] and the correlation of the critical viscosity values with the particle kinetic energy [64]. Recently, a modified critical viscosity model is proposed by Jiang *et al.* [65] considering the effect of the surface temperature in conjunction with the traditional particle viscosity. Therefore, the particle sticking probability is a result of the combination between two ratios, the first one related to the particle viscosity and critical viscosity value and the second one related to the surface temperature compared to the metal critical temperature.

Critical velocity method. This model is based on the comparison between a threshold value of velocity and the particle velocity [66]. The threshold value is strongly dependent on the particle material and mass. According to this model, particles stick to the surface when the velocity value is lower than a threshold (critical velocity). The formulation for the critical velocity calculation suggested in [66] is the following

$$\mathrm{v}_\mathrm{c}^2 = \frac{-1+f^2}{R^2}\frac{2W_\mathrm{A}}{m} \tag{3}$$

referred to the normal component of the impact velocity. The term W_A is the work of adhesion and R is the coefficient of restitution. The work of adhesion [67] could be expressed as

$$W_\mathrm{A} = -\left[\frac{5}{4}\rho\pi^{\frac{9}{2}}(k_1+k_2)\right]^{\frac{2}{5}}\gamma r^2|\mathrm{v}|^{\frac{4}{5}} \tag{4}$$

$$R = \frac{C}{C+|\mathrm{v}|^p} \tag{5}$$

where k_i is defined according to the Young modulus, E_Y, and Poisson's coefficient v, as

$$k_\mathrm{i} = \frac{1-\nu_\mathrm{i}^2}{\pi E_{\mathrm{Y,i}}} \tag{6}$$

and C and p are constants that can be derived from experimental tests. Also in this model, the particle properties such as the Young modulus are affected by the temperature, which varies dramatically at high temperature. The model is well suited to ash contamination in gas turbines using the following relation for the particle's Young modulus [68]

$$E_{\mathrm{Y,p}} = 120(1589-T)^3 \qquad for \;\; T > 1100\ \mathrm{K} \tag{7}$$

and in the case of coal-ash contamination [68] using

$$E_{\mathrm{Y,p}} = 3\cdot 10^{20}e^{(-0.02365\,T)} \tag{8}$$

Model constants were derived from experimental tests, obtained by fitting the experimental trends as a function of the particle temperature values.

The simplified relations of critical velocity and composite Young modulus are used in this model in order to study the gas turbine hot section fouling [69]. It is important to highlight that the dependency of the critical velocity model on the relationship between particle temperature and Young's modulus can determine a degree of inaccuracy. With this mode, only by knowing the precise relationship between particle Young modulus and temperature is it possible to obtain the proper prediction. Equations 8, 9 and 10 will be used for the data post-process in the following section.

$$\mathrm{v_c} = \left(\frac{2E_\mathrm{Y}}{d}\right)^{\frac{10}{7}} \tag{9}$$

$$E_\mathrm{Y} = 0.51\left(\frac{5\pi(k_1+k_2)}{4\rho^{3/4}}\right)^{\frac{2}{5}} \tag{10}$$

The impact mechanics are taken as a base for three recent new models. A deposition model that includes elastic deformation, plastic deformation, adhesion and shear removal is reported by Bons *et al.* [70]. Its predictions were compared to five literature cases: quartz

on aluminum, ash on stainless steel, sand on stainless steel, ash on Inconel at high temperature and ash on vane cascade. This model is used in the numerical analysis reported by [71] and [72] after proper model constant tuning.

The second one, is related to the numerical modeling of particle deposition that occurs in gas turbine hot sections over a wide temperature range [73]. This model is able to account for particle deposition from 500 K to 1500 K. The transition between these two extreme conditions is modeled through a temperature-driven modification of the mechanical properties of both particles and target surfaces.

The third method is proposed by Yu and Tafti [74] as a modification of the former model [75] and it is based on the relation between particle temperature and yield stress at high temperature starting from 1000 K. The model predictions were compared against experimental data realized with sand particles.

PREDICTIVE MODELS FOR PARTICLE CHARACTERISTICS

In order to apply the particle sticking models to the literature experimental data obtained for silica-based contaminants, particle viscosity and particle softening temperature values have to be estimated. Particle viscosity is dependent on particle composition and temperature while particle softening temperature is correlated only to the particle composition. In this section the models used in this work are briefly discussed, while a detailed description of the model equations and coefficients are reported in the Appendixes.

Particle viscosity model. The silica networks are defined

by the strong covalent bonding between atoms of silicon and oxygen. The silica network can accommodate different cations that can be grouped into three categories depending on the interaction of cations and network: (i) glass formers (Si^{4+}, Ti^{4+}, P^{5+}) which act as building blocks in the network, (ii) modifiers (Ca^{2+}, Mg^{2+}, Fe^{2+}, K^{+}, Na^{+}) which disrupt the polymer chains by bonding with oxygen and (iii) amphoterics (Al^{3+}, Fe^{3+}, B^{3+}) which act either as glass formers or as modifiers [76].

In this work, two viscosity models are considered. The first one is a very general method proposed by the National Physical Laboratory (called the NPL model) and it is used to calculate the particle viscosity. It can predict the particle viscosity based on the composition and temperature [77]. The applicability of the NPL method is not limited to certain compositions of the materials allowing a uniform comparison over the literature results. The NPL method and its correction [78, 79] are reported in Appendix A.

The second model is proposed by Giordano *et al.* [80] (GRD model) that predicts the viscosity of silicate melts as a function of temperature and melt composition, including the rheological important volatile constituents (such as water) at atmospheric pressure (10^5 Pa). This model is specifically designed for predicting the viscosity of volcanic ashes [38]. It is based on over one thousand five hundred (1500) measurements of viscosity on multicomponent anhydrous and volatile-rich silicate melts.

Journal of Engineering for Gas Turbines and Power. Received July 29, 2018;
Accepted manuscript posted August 27, 2018. doi:10.1115/1.4041282

The latter model will only be used for predicting the viscosity of particles for tests which involve volcanic ashes. The constitutive equations and the model coefficients are reported in Appendix B as well as the applicability limits in term of oxide weight fraction.

Particle softening model. The softening temperature is defined by ASTM – D1857-04 (*Standard test method for fusibility of coal and coke ash*) [81], as the temperature at which a triangular pyramid of material has fused down to a spherical particle which is characterized by the height equal to the width at the base. The softening temperature is considered as the critical temperature at which the critical viscosity is defined. In this paper, the model proposed by [82] is used to compute the ash softening temperature as a function of particle composition. The model relations are reported in Appendix C.

LITERATURE DATA COLLECTION

Data collection covers about thirty (30) years of particle deposition tests available in literature and allows the widest insight of particle deposition on gas turbine hot sections. Over seventy (70) particle deposition tests are collected.

The experimental results related to particle deposition on hot gas turbine sections are summarized in Table 1. For each test, details about particle (diameter and density) as well as the former name of the contaminant are reported. In the case of more contributions using the same material, with different test conditions, a progressive number is adopted. The particle dimension is reported as the variability range or the mean mass diameter used in each test (if provided). In the absence of detailed information, particle velocity is assumed equal to gas velocity as particle temperature is considered equal to gas temperature. For the tests realized on a full-scale gas turbine, a representative velocity of 100 m/s is assumed for particle impact, due to the lack of data related to this variable [19, 20].

For contaminants named lignite and PRB used in [45], particle density is calculated by means of the model reported in [83] coupled with the model constant provided in [84].

The chemical composition of contaminants is reported as a weight fraction of oxides (sodium oxide Na_2O, potassium oxide K_2O, calcium oxide CaO, magnesium oxide MgO, silicon dioxide SiO_2, aluminum trioxide Al_2O_3, titanium dioxide TiO_2 and iron trioxide Fe_2O_3). This classification does not cover the entire composition for each material, but these components characterize each contaminant determining their physical characteristics.

Material characterization is often reported but sometimes it is not complete or, in the worst cases, completely absent. Material characterization is fundamental for calculating physical properties (e.g. viscosity, softening temperature, etc.) directly related to the particle adhesion phenomenon. In this paper, two material characterizations related to volcanic rock, are taken from literature. The composition of Twin Mountain basaltic rock St. Helens rock is taken from literature in [85] and [86] respectively.

The target types (TT) used in the experimental tests are also reported in Table 1 with the following references:

- T, the test is performed on full scale gas turbines;

- B, the test is performed on wind tunnels provided with cascade or single blade targets;
- C, the test is performed using a coupon;
- I, the test is performed in order to discover particle deposition inside the internal cooling hole.

The uncertainty related to the experimental test conditions and in turn, the accuracy of the particle deposition results is not easily found in literature even if a considerable number of tests indicate the uncertain magnitude. Difficulties are especially related to the unclear correlation between the uncertainties related to test conditions (such as velocity and temperature) with mass deposits or sticking coefficients.

Uncertainties related to the temperature values are about 0.11 % [51], 1.3 % [30] and 2 % [44, 45, 47, 48], while the uncertainties related to the mass flow rate, that could be used to estimate the uncertainty in the particle impact velocity, are about 0.80 % [51] and 4 % [29, 45, 47, 48]. Coolant flow is affected by uncertainty as well, quantified in 12 % in [47]. In relation to the variability of the test conditions during the deposition tests, the variability of the flow temperature is comprised within 3 K [48], 5 K in [53] and 6 K [45], while the variability of the mass flow rate is comprised within 0.005 kg/s [48] and 0.01 kg/s [45]. Other inaccuracies are especially related to the effects of radiation on the flow temperature measures [24, 30, 61].

Using the literature data as a "black-box" particular effects and/or uncertainties related to the experimental tests were neglected. The difference in temperature of the target surface, impact angle and stagnation effects in front of the target could determine the variation of the particle behavior upon impact. As reported by Guha [87], the temperature gradient near walls affects particle deposition especially for smaller particles. In this review some of the considered cases present cooled coupons and/or cooled blades as well as several tests performed without specific surface temperature control. In the same way, surface roughness modifies (increases) particle deposition rate but unfortunately no detailed information was reported in the correspondent reference.

For these reasons, this data collection and the subsequent data post-process reported in the following sections ensures the understanding of the basic phenomena using order of magnitude variation giving inspiration for further analyses able to consider all of the aforementioned important aspects.

Preliminary analysis. The data reported in Table 1 provide the first overview of the experimental contributions related to particle deposition and fouling on gas turbine hot sections. From these data, several analyses can be performed. In this section, a preliminary analysis of the test conditions is reported.

Figure 1 shows the number of occurrences for particle diameter, velocity and temperature. This data visualization allows the comprehension of the state of the art and possible lack of experimental test conditions: particle velocity changes in the range from 15

m/s to 310 m/s while the temperature values range from 900 K to 1950 K, approximately. Particle diameter is quite spread even if, numerous contributions involve particles in the range from 5 μm to 20 μm.

Starting from this detailed information, the particle Stokes number and the particle relaxation time can be calculated. In Appendix D data about the geometrical features of the target for each experimental test are reported. Particle Stokes number and particle relaxation time are listed in relation to the airflow characteristics calculated assuming pure air as a carrier gas with characteristics calculated according to CoolProp library [90].

Particle viscosity. Based on the chemical composition of the material, particle viscosity is calculated as a function of temperature using the NPL model. Different materials at several temperatures are tested and the results are compared in terms of viscosity. As shown in Figure 2, the variation of particle viscosity is almost six (6) orders of magnitude for lower temperature and three (3) orders of magnitude for higher temperature while most of the data is localized in the range of $(1 - 10^4)$ Pa s. Even if the particle sticking capability can be related to the particle condition (solid, semi-molten or molten) this first comparison shows the huge variability of the viscosity values over the considered tests.

According to the critical viscosity model, the capability of each particle to adhere can be evaluated by using particle viscosity and the critical viscosity values. Critical viscosity could be calculated as a function of the softening temperature T_{soft} that is assessed according to the compositions of the materials. Table 2 shows the softening temperature for all materials listed in Table 1 calculated according to the model reported by Yin *et al.* [82].

The viscosity ratio (μ/μ_c) trends according to the temperature values are reported in Figure 3. According to the critical viscosity method, two regions for each material can be defined according to the viscosity ratio (μ/μ_c) identifying the sticky and the rebound condition. As can be seen in Figure 3, experimental tests are mainly conducted in the sticky regions excluding a few cases in which the results of test conditions lie inside the rebound region due to the lower particle temperature of deposition tests. Figure 3 reports all data belonging to different sources such as volcanic, coal and silty particles and, at the same time, only the NPL method is applied for calculating the viscosity ratio. In the following analysis, a distinction between these tests is proposed according to the viscosity method. At the same time, the softening temperature is calculated with the same aforementioned model [82].

The first analysis, reported in Figure 4, shows silty and coal particle tests. In this case, silty particle tests mainly belong to the rebound region, while coal particle tests are located in the sticky region even if, some of these tests are conducted with the same temperature as silty tests. This difference is due to the different relationship between particle viscosity and temperature generated by the different chemical compositions. As reported by [91], differences in chemical composition must be taken into account and the similarities between different particle impact tests have to be drawn considering these differences. In light of this, the viscosity method proposed by Giordano

et al. [80] is only applied to the volcanic ash tests. According to the chemical classification proposed in [92], Figure 5 reports the Total Alkali-Silica (TAS) diagram with the superimposition of the twelve (12) volcanic ashes considered in this review. Tests can be classified according to six different categories called basalt, basaltic-andesite, dacite, rhyolite, basaltic trachy-andesite and trachydacite. These subalkaline series are characterized by a lower amount of alkali and a progressive increase in silica dioxide content and are included in the GRD model.

Figure 6 reports the viscosity ratio as a function of the temperature for volcanic ashes using the GRD method [80]. Twelve (12) tests out of seventeen (17) are shown. Laki 2, 3, 4 and 5 and Twin Mountain tests are characterized by a particle composition out of the validity range indicated by Giordano *et al.* [80]. Also in this case, several tests are located in the rebound region where the sticking model fails the predictions. As mentioned above, by using different viscosity prediction models, the viscosity ratio (μ/μ_c) can vary noticeably. Figure 7 shows the comparison between the critical viscosity ratio calculated according to the NPL and the GRD viscosity method. The comparison highlights how the choice of

the viscosity model affects the particle adhesion prediction. It can be noted that predictions are not aligned with the straight dashed line (provided as reference for the reader), but the trends change according to the tests and according to the viscosity ratio μ/μ_c. This evidence has to be matched with the trends reported in Figure 2: by changing the test temperature by 50 K, the particle viscosity may change by an order of magnitude and, by considering the different relation between viscosity and temperature, this could imply different predictions in terms of particle sticking or rebound.

This analysis shows how important the correct estimation of particle temperature is, as well as the choice of the viscosity evaluation model and sticking model in the prediction of particle adhesion and/or rebound.

Particle velocity. This analysis is carried out using Eq. (10) for the calculation of the Young modulus and using Eq. (9) as a reference. The Young modulus of the surface is set equal to 200 GPa, while the Poisson coefficient is equal to 0.3 for both particle and surface. The Young modulus for the particle

is calculated according to Eq. (8) that is suitable for coal-ash contamination. Figure 8 shows the comparison between a representative test (JBPS B 2) condition at v = 79 m/s and the consequent critical velocity. The dashed line in the picture is representative of the particle velocity used in the tests and the critical velocity is reported as a function of temperature and diameter. In this case, the overall range of particle diameter (2 – 20) µm, instead of the mass mean average diameter equal to 11.6 µm has been considered. In the same way, a temperature values in the range of 1273 K 1373 K instead of single temperature value equal to 1366 K have been considered for the analysis. This assumption is based on the experimental evaluations reported in [46]. The Authors in [46] reported the temperature map across the vane, showing a non-uniform temperature pattern. If the particle velocity is lower than the critical velocity value, the particle

is able to stick to a surface. Taking into consideration the critical velocity trends, for a given particle diameter, the particle velocity range for which the particle is able to stick increases according to temperature

values. This trend is related to Young modulus variation with temperature (see Eq. 8). Analogous results can be obtained by fixing particle temperature and decreasing particle diameter. In this case, the critical velocity value is inversely proportional to the particle diameter (see Eq. 9).

As can be predicted by the critical velocity model, particle adhesion occurs in the case of smaller diameter and higher temperature values. In this case, according to the critical velocity model, several experimental conditions lie outside the adhesion region. In this case, the actual non-uniform temperature pattern, instead of the single value taken as the reference for this test, show how for a single adhesion test, different results may occur as a function of the local flow conditions.

Neither the critical viscosity nor the velocity method can predict particle sticking for the overall particle adhesion tests. The mismatch between the prediction and the actual result of the test can be explained by two reasons. For a specific test, deposits are generated by a certain combination of particle diameter, temperature and velocity and therefore, by considering the overall variation of these quantities during tests, some conditions may generate particle rebound. At the same time, particle characteristics such as viscosity and softening temperature are difficult to represent by a single model able to conceive a wide range of particle chemical compositions.

Summing up, a particle impact test reporting adhesion, can be the outcome of multiple superimposed effects in terms of particle size, temperature and impact conditions.

PARTICLE IMPACT BEHAVIOR MAP

Referring to the experimental data reported in Table 1, Figure 9 gathers all the test results. The data are organized according to particle kinetic energy E_{kin}

$$E_{\text{kin}} = \frac{1}{2} m v^2 \tag{11}$$

and the ratio between particle temperature and the softening temperature Θ.

$$\Theta = T/T_{\text{soft}} \tag{12}$$

Given the values of particle diameter and velocity, the particle impact behavior that characterizes the experimental data is driven by inertia and for this reason, the particle kinetic energy is suitable to represent the particle dynamics during the impact. In addition, Θ represents an estimation of the particle state (solid or liquid) avoiding the calculation of the viscosity value. This assumption is based on evidence from literature. As reported in [91] volcanic ash for example, softens at a lower temperature than crystalline silicates and, for the same gas temperature, the use of standard materials (MIL E 5007C test sand) as reference dust instead of the actual volcanic ash

determines incorrect results. In addition, the standard procedures for the calculation of material viscosity are affected by several inaccuracies, and the comparison of different methods is not straightforward [93 – 97]. At the same time, a standard procedure exists for the determination of the softening temperature [81] suitable for estimating the material characteristics with a proper confidence band.

By using the relation proposed by Yin *et al.* [82], unavoidable inaccuracy affects the data post-process due to the impossibility to directly evaluate the particle softening temperature. However, this post-process aims to focus on all the parameters that actually influence the calculation of particle sticking characteristics.

As can be seen in Figure 9, data are localized across $\Theta = 1 \pm 0.2$, even if some experimental tests are characterized by Θ values up to 1.6. Regarding kinetic energy, the experimental data cover almost six (6) orders of magnitude from 1e-5 J to 1e-11 J. The data characterized by lower values of kinetic energy (1e-13 J – 1e-15 J) correspond to the lower limit of particle diameter range used in the test (ARD 3, 5 6; Arkwright, 2; Blue Gem, 2; AMAX, Otisca coal and Coal) while the data characterized by higher values (Laki 5) display higher velocity (365 m/s) and higher particle diameter (up to 100 μm).

The deposition data reported in Figure 9 can be combined with experimental data related to other types of phenomena involved in gas turbine operation in the presence of contaminants such as erosion and particle breaking/splashing.

Table 3 summarizes the erosion data reported in [55 – 57] as well as the softening temperature calculated according to the model of Yin *et al.* [82]. Erosion and sticking are due to the same type of particles (rock-derived particles and coal contaminants) and, sometimes, affect the hot gas turbine section simultaneously. Dedicated test rigs were used for evaluating the erosion of the blade surface in hot conditions. By analyzing the temperature values reported in Table 3 it is clear how, for the same materials, velocity and diameter, the erosion problem takes place for lower temperatures than those that determine particle deposition. In addition, Table 3 reports a test conducted with volcanic ash (Laki 6) reported by Shinozaky *et al.* [21]. This test is carried out with the same experimental setup as the test called Laki 5 reported in Table 1 but in this case, no deposition occurs. The tests are performed with lower rotational speed and a lower temperature that determines particle rebound instead of particle adhesion.

Table 4 summarizes the experimental conditions at which particle splashing occurs. The materials are among the ones previously used for particle deposition tests but, in this case, the tests are characterized by higher particle diameter. Also in this case, softening temperature is calculated according to [82]. These tests were carried out with spherical-pellets of volcanic ash fired towards a flat surface. Particle splashing was verified by a digital image provided by the Authors [37]. Even if this information is qualitative, splashing is the only effect reported and no data related to erosion or deposition are reported.

The data reported in Table 3 and 4 are added to the E_{kin}-Θ plane reported in Figure 10 where the data related to the deposition tests (see Table 1) are marked with grey dots.

The erosion/rebound data are characterized by lower values of Θ and slightly higher kinetic energy values with respect to the deposition tests. Erosion/rebound tests are carried out with the same materials as for the deposition tests, but the lower temperature values and sometimes, the combination of particle diameter and velocity (that determines higher values of kinetic energy) leads to the erosion issues.

Starting from these considerations and the data reported in Table 1, Table 3 and Table 4, Figure 11 shows the particle impact behavior map. The regions reported in this map are the results of over thirty (30) years and seventy (70) experimental particle depositions, erosion and splashing tests. Each region depicted in the map, is related to evidence from literature reported in the following description.

Deposition. This region is based on the data reported in Table 1. The combination of particle temperature and softening temperature allows the dissipation of the impact energy by particle deformation determining adhesion. Particles with these characteristics are too soft to cause erosion issues and do not have enough kinetic energy to determine the splashing phenomenon. The erosion phenomenon is related to the strength of the surface that strongly depends on the temperature values [98 – 100] and for this reason, a certain superimposition between the deposition/erosion region has to be considered. Finally, in the case of particles characterized by very low kinetic energy particles could roll and slip on the surface without notable sticking.

Erosion/Rebound. The particle kinetic energy still makes it subject to sticking but particles may not be sufficiently soft. For lower temperatures, the erosion severity depends on the particle characteristics and surface strength. Experimental tests reported in [101] were characterized by Θ = 0.54 and E_{kin} = 3e-7 J and no particle sticking was detected. In the intersection with the *Deposition* region (comprised in the range of Θ equal to 0.8 – 1.0) the dual effect of particle impact becomes predominant. As reported in [23], particles are sufficiently soft to determine adhesion, but can determine erosion phenomena as well. Experimental tests carried out under these conditions should consider the contemporary presence of particle sticking and erosion. In light of this, the results of these tests may not be suitable for generating/validating sticking/erosion models.

As the particle kinetic energy increases, particle erosion become even more severe, in particular for lower values of Θ. In this condition erosion and particle fragmentation take place. Particle fragmentation is an energy dissipation phenomenon due to the remaining part of kinetic energy not dissipated by the deformation process [102, 103]. As kinetic energy increases, particle fragmentation increases as well.

Erosion/Splashing. Tests resulting in particle splashing are characterized by higher values of kinetic energy than deposition and erosion tests (up to ten (10) order of magnitude) due to the higher particle diameter. The kinetic energy associated with the velocity and particle mass may not entirely dissipated by particle deformation upon impact resulting in particle break and thus splashing. According to the frames of the impact reported in [37], particle splashing generates a large number of smaller particles after the primary impact

which could be re-entrained by the core flow re-impacting on the surface with lower velocity and residual elasticity of the silica networks. For high values of kinetic energy, part of this energy is dissipated by particle breaking. When a particle is too soft ($\Theta > 1$) and it impacts on the surface at high kinetic energy, the deformation process determines particle splashing as reported in [37]. Particle splashing generates smaller semi-molten particles that could determine deposits in the case of secondary impacts [104]. Successive impacts are characterized by lower values of kinetic energy determining more favorable sticking conditions (*Deposition* region).

No data. This particular region does not represent a specific result of particle impact, but some considerations can be made. Lower values of E_{kin} and Θ do not determine particle deposition or erosion even if, these conditions are representative of particular conditions for which particle adhesion occurs.

The first particular condition is described well by Sacco *et al.* [105]. In this experimental test, the ARD particles impact the surface of the internal cooling holes with very low velocity and significantly low temperature (< 728 K). In these conditions, some particles are trapped in recirculating and stagnation zones and they repeatedly impact the hot surface at low velocity [105].

The second condition refers to the particle impact that occurs in the compressor sections. Sub-micro-sized solid particles are a class of particles that determines compressor fouling [1], or in other words, these particles stick under cold conditions. As reported in literature, compressor fouling is promoted by the presence of third substances at the particle surface interface [106, 107] and for these reasons, the adhesion capability that characterizes this region, could be due to the effects of particular surface conditions. Unfortunately, detailed experimental analyses are not reported in literature. A small number of contributions (compared to those reported for hot sections) involved particle sticking analysis relate to cold conditions. On-field detections [107, 108] have revealed that only the first stages are affected by deposits and are driven by the presence of liquid water at the particle surface interface. Regarding wind tunnel tests, Kurz *et al.* [109] reported an experimental investigation which provides experimental data on the amount of foulants in the air that stick to a blade surface under dry and humid conditions. The tests show a higher deposition rate provided by wet surfaces compared to dry ones. Similar results are reported in [110] where glue agents on the blade surface enhance the particle adhesion rate dramatically.

In hot sections, glue agents are described with the name of vapor deposition [17, 60, 111]. This phenomenon, due to the presence of a condensed phase downstream the combustor sections, can increase the sticking capabilities of nanoparticles (mass mean diameter < 0.1 μm) dragged in the vicinity of the surface by diffusion and thermophoresis forces.

The proposed map is based on a data post-process of the literature experimental tests. The impact behavior map allows a direct comparison between the historical tests as well as allowing the prediction of the results of a generic particle impact based on the experimental evidence obtained with several independent tests and measurements.

CONCLUSIONS

This paper reports a collection of over seventy (70) experimental tests realized over thirty (30) years and carried out for studying particle deposition on hot gas turbine sections. These tests involved several different silica-based materials, from volcanic ashes to coal contaminants covering fouling issues of aero engines and land-based power units.

Starting from these data, a sensitive analysis related to particle characteristics (such as particle viscosity and softening temperature) has shown that the comparison of different tests is not straightforward. Different materials melt at different temperatures as well as the viscosity-temperature trends which vary according to their composition.

The application of literature sticking models (such as critical viscosity and critical velocity methods) to the collected experimental data has shown how, in some cases, model predictions and the experimental results are in contrast. Predictions of particle sticking appear to be related to the adopted viscosity method and, in turn, numerical analysis that involves one method instead of another, could fail the proper prediction of particle sticking or rebound.

Furthermore, the comparison has shown two main issues: particle sticking models have to be improved in order to follow the different chemical composition of particles and the different flow conditions and, experimental data (conditions, materials and results) have to be reported more precisely and in greater detail in order to apply the models (for particle viscosity, softening and sticking characteristics) with the highest confidence.

Additional experimental tests involving erosion and splashing as a result of particle impact were added to the analysis to define the general behavior of particle impact.

Comparing particle kinetic energy to the ratio of particle temperature and softening temperature, three (3) main impact behaviors can be assessed. The impact effects were recognized according to various evidence reported in literature, and a dimensional predictive map was created including deposition, erosion, rebound, splashing and fragmentation.

In light of this, the predictive map proposed in this paper is based on several different experimental tests realized over three decades. Methodologies, technologies and uncertainties were developed over the years and therefore, this comparison is performed by order of magnitude. From this analysis, perspectives and possibilities for further investigations can be drawn, in relation to (i) the limitations of the sticking models and (ii) the lack of experimental results for a specific combination of particle kinetic energy and the ratio of particle temperature and softening temperature. All the future data can be added to this map, representing an up-to-date reference database for the community.

NOMENCLATURE

A	model coefficient	
a	model constant	
B	model coefficient	
C	model constant/coefficient	
d	particle diameter	[m]
E	energy	[J]
E_Y	Young Modulus	[Pa]
F	frequency (number of occurrences)	[-]
f	friction	[-]
k	coefficient (ref. to material properties)	[m^2/N]
L	characteristic length	[m]
m	particle mass	[kg]
n	number of oxygen atoms in the molecule	[-]
P	sticking probability	[-]
p	model constant	
R	coefficient of restitution	[-]
r	radius	[m]
St	particle Stokes number	[-]
T	temperature	[K]
v	velocity	[m/s]
W	work (referred to the adhesion)	[J]

Greek letters

Θ	temperature ratio	[-]
Λ	optical basicity	[-]
μ	viscosity	[Pa s]
v	Poisson's coefficient	[-]
ρ	density	[kg/m^3]

τ	particle relaxation time	[s]
χ	mole fraction	[-]

Subscripts and superscripts

A	adhesion
c	critical
C	corrected
g	gas
i	index
kin	kinetic
NC	non-corrected
p	particle
soft	softening (referred to the particle behavior)
visc	viscosity

Acronyms

B	Blade or cascade (referred to the target)
C	Coupon
GRD	Giordano Russell Dingwell (ref. to viscosity model)
I	Internal cooling passages
NPL	National Physical Laboratory (ref. to viscosity model)
T	Turbine
TT	Type of Target

REFERENCES

[1] Suman A., Morini M., Aldi N., Casari N., Pinelli M., Spina P.R. A compressor fouling review based on an historical survey of asme turbo expo papers (2017) Journal of Turbomachinery, 139 (4), art. no. 041005. DOI: 10.1115/1.4035070.

[2] Clarkson R.J., Majewicz E.J.E., Mack P. A re-evaluation of the 2010 quantitative understanding of the effects volcanic ash has on gas turbine engines (2016) Proceedings of the Institution of Mechanical Engineers, Part G: Journal of Aerospace Engineering, 230 (12), pp. 2274–2291. DOI: 10.1177/0954410015623372.

[3] Dunn M.G. Operation of gas turbine engines in an environment contaminated with volcanic ash (2012) Journal of Turbomachinery, 134 (5), art. No. 051001. DOI: 10.1115/1.4006236.

[4] De Giorgi M.G., Campilongo S., Ficarella A. Predictions of operational degradation of the fan stage of an aircraft engine due to particulate ingestion (2015) Journal of Engineering for Gas Turbines and Power, 137 (5), art. no. 052603. DOI: 10.1115/1.4028769.

[5] Allaby M. A Dictionary of Geology and Earth Sciences. Oxford, UK: Oxford University Press; 2013.

[6] Cohn A. Effect of gas and metal temperatures on gas turbine deposition (1982) American Society of Mechanical Engineers (Paper), 11 p. DOI: 10.1115/82-JPGC-GT-4.

[7] Whitlow G.A., Lee S.Y., Mulik P.R., Wenglarz R.A., Sherlock T.P., Cohn A. Combustion turbine deposition observations from residual and simulated residual oil studies (1983) Journal of Engineering for Gas Turbines and Power, 105 (1), pp. 88–96. DOI: 10.1115/1.3227403.

[8] Wenglarz R.A., Cohn A. Turbine deposition evaluations using simplified tests (1983) American Society of Mechanical Engineers (Paper), p. 7. DOI: 10.1115/83-GT-115.

[9] Wenglarz R.A. Turbine disposition, erosion and corrosion evaluations using a simplified test approach (1987) American Society of Mechanical Engineers (Paper), p. 7. DOI: 10.1115/87-GT-214.

[10] Wenglarz R.A. Direct coal-fueled combustion turbines (1987) American Society of Mechanical Engineers (Paper), p. 8. DOI: 10.1115/87-GT-269.

[11] Kimura S.G., Spiro C.L., Chen C.C. Combustion and deposition in coal-fired turbines (1987) Journal of Engineering for Gas Turbines and Power, 109 (3), pp. 319–324. DOI: 10.1115/1.3240042.

[12] Spiro C.L., Kimura S.G., Chen C.C. Ash behavior during combustion and deposition in coal-fueled gas turbines (1987) Journal of Engineering for Gas Turbines and Power, 109 (3), pp. 325–330. DOI: 10.1115/1.3240043.

[13] Wenglarz R.A., Fox Jr R.G. Physical aspects of deposition from coal-water fuels under gas turbine conditions (1990a) Journal of Engineering for Gas Turbines and Power, 112 (1), pp. 9–14. DOI: 10.1115/1.2906484.

[14] Wenglarz R.A., Fox Jr R.G. Chemical aspects of deposition/corrosion from coal-water fuels under gas turbine conditions (1990b) Journal of Engineering for Gas Turbines and Power, 112 (1), pp. 1–8. DOI: 10.1115/1.2906471.

[15] Wenglarz R.A. An approach for evaluation of gas turbine deposition (1992) Journal of Engineering for Gas Turbines and Power, 114 (2), pp. 230–234. DOI: 10.1115/1.2906577.

[16] Chin J.S., Lefebvre A.H. Influence of flow conditions on deposits from heated hydrocarbon fuels (1993) Journal of Engineering for Gas Turbines and Power, 115 (3), pp. 433–438. DOI: 10.1115/1.2906727.

[17] Nagarajan R., Anderson R.J. Effect of coal constituents on the liquid-assisted capture of impacting ash particles in direct coal-fired gas turbines (1988) Proceedings of the ASME Turbo Expo, 3. DOI: 10.1115/88-GT-192.

[18] Dunn M.G., Padova C., Moeller J.E., Adams R.M. Performance deterioration of a turbofan and a turbojet engine upon exposure to a dust environment (1987) Journal of Engineering for Gas Turbines and Power, 109 (3), pp. 336–343. DOI: 10.1115/1.3240045.

[19] Kim J., Dunn M.G., Baran A.J., Wade D.P., Tremba E.L. Deposition of volcanic materials in the hot sections of two gas turbine engines (1993) Journal of Engineering for Gas Turbines and Power, 115 (3), pp. 641–651. DOI: 10.1115/1.2906754.

[20] Dunn M.G., Baran A.J., Miatech J. Operation of gas turbine engines in volcanic ash clouds (1996) Journal of Engineering for Gas Turbines and Power, 118 (4), pp. 724–731. DOI: 10.1115/1.2816987.

[21] Shinozaki M., Roberts K.A., Van De Goor B., William Clyne T. Deposition of ingested volcanic ash on surfaces in the turbine of a small jet engine (2013) Advanced Engineering Materials, 15 (10), pp. 986-994. DOI: 10.1002/adem.201200357.

[22] Anderson R.J., Romanowsky C.J., France J.E. The Adherence of Ash Particles from the Combustion of Micronized Coal. Morgantown Energy Technology Center, Res. Rep. DOE/METC-85/2007 (DE85008600); October, 1984.

[23] Ross J.S., Anderson R.J., Nagarajan R. Effect of Sodium on Deposition in a Simulated Combustion Gas Turbine Environment (1988) Energy and Fuels, 2 (3), pp. 282–289. DOI: 10.1021/ef00009a010.

[24] Anderson R.J., Logan R.G., Meyer C.T., Dennis R.A. A combustion/deposition entrained reactor for high-temperature/pressure studies of coal and coal minerals (1990) Review of Scientific Instruments, 61 (4), pp. 1294–1302. DOI: 10.1063/1.1141176.

[25] Richards G.A., Logan R.G., Meyer C.T., Anderson R.J. Ash deposition at coal-fired gas turbine conditions: Surface and combustion temperature effects (1992) Journal of Engineering for Gas Turbines and Power, 114 (1), pp. 132–138. DOI: 10.1115/1.2906295.

[26] Weaver M.M., Dunn M.G., Heffernan T. Experimental determination of the influence of foreign particle ingestion on the behavior of hot-section components including Lamilloy (1996) American Society of Mechanical Engineers (Paper), pp. 10. DOI: 10.1115/96-GT-337.

[27] Jensen J.W., Squire S.W., Bons J.P., Fletcher T.H. Simulated land-based turbine deposits generated in an accelerated deposition facility (2005) Journal of Turbomachinery, 127 (3), pp. 462–470. DOI: 10.1115/1.1860380.

[28] Bons J.P., Crosby J., Wammack J.E., Bentley B.I., Fletcher T.H. High-pressure turbine deposition in land-based gas turbines from various synfuels (2007) Journal of Engineering for Gas Turbines and Power, 129 (1), pp. 135–143. DOI: 10.1115/1.2181181.

[29] Wammack J.E., Crosby J., Fletcher D., Bons J.P., Fletcher TH. Evolution of Surface Deposits on a High Pressure Turbine Blade, Part I: Physical Characteristics (2008) Journal of Turbomachinery, 130 (2), art. no. 021020. DOI: 10.1115/1.2752182.

[30] Crosby J.M., Lewis S., Bons J.P., Ai W., Fletcher T.H. Effects of Temperature and Particle Size on Deposition in Land Based Turbines (2008) Journal of Engineering for Gas Turbines and Power;130 (5), art. no. 051503. DOI: 10.1115/1.2903901

[31] Ai W., Laycock R.G., Rappleye D.S., Fletcher T.H., Bons J.P. Effect of particle size and trench configuration on deposition from fine coal flyash near film cooling holes (2011) Energy and Fuels, 25 (3), pp. 1066–1076. DOI: 10.1021/ef101375g.

[32] Ai W., Murray N., Fletcher T.H., Harding S., Lewis S., Bons J.P. Deposition near film cooling holes on a high pressure turbine vane (2012) Journal of Turbomachinery, 134 (4), art. no. 041013. DOI: 10.1115/1.4003672.

[33] Ai W., Murray N., Fletcher T.H., Harding S., Bons J.P. Effect of hole spacing on deposition of fine coal flyash near film cooling holes (2012) Journal of Turbomachinery, 134 (4), art. no. 041021. DOI: 10.1115/1.4003717.

[34] Laycock R.G., Fletcher T.H. Time-Dependent Deposition Characteristics of Fine Coal Fly Ash in a Laboratory Gas Turbine Environment. (2013) Journal of Turbomachinery, 135 (2), art. no. 021003. DOI: 10.1115/1.4006639.

[35] Laycock R., Fletcher T.H. Independent effects of surface and gas temperature on coal fly ash deposition in gas turbines at temperatures up to 1400 °C (2016) Journal of Engineering for Gas Turbines and Power, 138 (2), art. no. 2429919. DOI: 10.1115/1.4031318.

[36] Boulanger A., Patel H., Hutchinson J., DeShong W., Xu W., Ng W., Ekkad S. Preliminary experimental investigation of initial onset of sand deposition in the turbine section of gas turbines (2016) Proceedings of the ASME Turbo Expo, 1. DOI: 10.1115/GT2016-56059.

[37] Dean J., Taltavull C., Clyne T. Influence of the composition and viscosity of volcanic ashes on their adhesion within gas turbine aeroengines (2016) Acta Materialia, 109, pp. 8–16. DOI: 10.1016/j.actamat.2016.02.011.

[38] Giehl C., Brooker R.A., Marxer H., Nowak M. An experimental simulation of volcanic ash deposition in gas turbines and implications for jet engine safety (2017) Chemical Geology, 461, pp. 160–170. DOI: 10.1016/j.chemgeo.2016.11.024.

[39] Taltavull C., Dean J., Clyne T.W Adhesion of volcanic ash particles under controlled conditions and implications for their deposition in gas turbines (2016) Advanced Engineering Materials, 18 (5), pp. 803–813. DOI: 10.1002/adem.201500371.

[40] Barker B., Hsu K., Varney B., Boulanger A., Hutchinson J., Ng W.F. An experiment-based sticking model for heated sand (2017) Proceedings of the ASME Turbo Expo, 2D-2017. DOI: 10.1115/GT2017-64421.

[41] Boulanger A., Hutchinson J., Ng W.F., Ekkad S.V., Keefe M.J., Xu W., Barker B., Hsu K. Experimental based empirical model of the initial onset of sand deposits on hastelloy-X from 1000°C to 1100°C using particle tracking (2017) Proceedings of the ASME Turbo Expo, 2D-2017. DOI: 10.1115/GT2017-64480.

[42] Raj R. Deposition results of a transpiration air-cooled turbine vane cascade in a contaminated gas stream. (1983) Journal of Engineering for Gas Turbines and Power, 105 (4), pp. 826–833. DOI: 10.1115/1.3227488.

[43] Raj R., Moskowitz S. Experimental studies of deposition by electrostatic charge on turbine blades (1984) American Society of Mechanical Engineers (Paper). DOI: 10.1115/84-GT-159.

[44] Smith C., Barker B., Clum C., Bons J.P. Deposition in a turbine cascade with combusting flow (2010) Proceedings of the ASME Turbo Expo, 4 (Parts A and B), pp. 743–751. DOI: 10.1115/GT2010-22855.

[45] Webb J., Casaday B., Barker B., Bons J.P., Gledhill A.D., Padture N.P. Coal Ash Deposition on Nozzle Guide Vanes: Part I - Experimental Characteristics of Four Coal Ash Types (2012) Journal of Turbomachinery, 135 (2), art. no. 021033. DOI: 10.1115/1.4006571.

[46] Casaday B.P., Prenter R, Bonilla C, Lawrence M, Clum C, Ameri A, Bons JP. Deposition with Hot Streaks in an Uncooled Turbine Vane Passage. J Turbomach 2013;136:041017

[47] Prenter R., Whitaker S.M., Ameri A., Bons J.P. The effects of slot film cooling on deposition on a nozzle guide vane (2014) Proceedings of the ASME Turbo Expo, 3A. DOI: 10.1115/GT2014-27171.

[48] Whitaker S.M., Prenter R., Bons J.P. T The effect of freestream turbulence on deposition for nozzle guide vanes (2015) Journal of Turbomachinery, 137 (12), art. no. 121001. DOI: 10.1115/1.4031447.

[49] Lundgreen R., Sacco C., Prenter R., Bons J.P. Temperature effects on nozzle guide vane deposition in a new turbine cascade rig (2016) Proceedings of the ASME Turbo Expo, 5A-2016. DOI: 10.1115/GT2016-57560.

[50] Wang X.Y., Pu J., Yuan R.M., Wang J.H. Combined influence of surface deposition and hole-blockage on film-cooling performances (2016) Proceedings of the ASME Turbo Expo, 5C-2016. DOI: 10.1115/GT2016-56902.

[51] Wylie S., Bucknell A., Forsyth P., McGilvray M., Gillespie D.R.H. Reduction in flow parameter resulting from volcanic ash deposition in engine representative cooling passages (2017) Journal of Turbomachinery, 139 (3), art. no. 031008. DOI: 10.1115/1.4034939.

[52] Whitaker S.M., Lundgreen R.K., Bons J.P. Effects of metal surface temperature on deposition-induced flow blockage in a vane leading edge cooling geometry (2017) Proceedings of the ASME Turbo Expo, 2D-2017. DOI: 10.1115/GT2017-64946.

[53] Whitaker S.M., Peterson B., Miller A.F., Bons J.P. The effect of particle loading, size, and temperature on deposition in a vane leading edge impingement cooling geometry (2016) Proceedings of the ASME Turbo Expo, 5B-2016. DOI: 10.1115/GT2016-57413.

[54] Bunker R.S. Evolution of turbine cooling (2017) Proceedings of the ASME Turbo Expo, 1. DOI: 10.1115/GT2017-63205.

[55] Kotwal R., Tabakoff W. A new approach for erosion prediction due to fly ash (1981) Journal of engineering for power, 103 (2), pp. 265–270. DOI: 10.1115/1.3230716.

[56] Tabakoff W. Review-turbomachinery performance deterioration exposed to solid particulates environment (1984) Journal of Fluids Engineering, Transactions of the ASME, 106 (2), pp. 125–134. DOI: 10.1115/1.3243088.

[57] Tabakoff W., Hamed A., Metwally M., Pasin M. High-temperature erosion resistance of coatings for gas turbine (1992) Journal of Engineering for Gas Turbines and Power, 114 (2), pp. 242–249. DOI: 10.1115/1.2906579.

[58] Mezheritsky A.D., Sudarev A.V. The mechanism of fouling and the cleaning technique in application to flow parts of the power generation plant compressors (1990) Proceedings of the ASME Turbo Expo, 4. DOI: 10.1115/90-GT-103.

[59] Senior C.L., Srinivasachar S. Viscosity of Ash Particles in Combustion Systems for Prediction of Particle Sticking (1995) Energy and Fuels, 9 (2), pp. 277–283. DOI: 10.1021/ef00050a010.

[60] Ahluwalia R.K., Im K.H., Chuang C.F., Hajduk J.C. Particle and Vapor Deposition in Coal-Fired Gas Turbines. (1986) ASME Paper, 86-GT-239. DOI:10.1115/86-GT-239.

[61] Ahluwalia R.K., Im K.H., Wenglarz R.A. Flyash adhesion in simulated coal-fired gas turbine environment (1989) Journal of Engineering for Gas Turbines and Power, 111 (4), pp. 672–678. DOI: 10.1115/1.3240311.

[62] Sreedharan S.S., Tafti D.K. Composition dependent model for the prediction of syngas ash deposition in turbine gas hotpath (2011) International Journal of Heat and Fluid Flow, 32 (1), pp. 201–211. DOI: 10.1016/j.ijheatfluidflow.2010.10.006.

[63] Singh S., Tafti D.K. Prediction of Sand Transport and Deposition in a Two-Pass Internal Cooling Duct (2016) Journal of Engineering for Gas Turbines and Power, 138 (7), art. no. 072606. DOI: 10.1115/1.4032340.

[64] Srinivasachar S., Helble J.J., Boni A. An experimental study of the inertial deposition of ash under coal combustion conditions (1991) Symposium (International) on Combustion, 23 (1), pp. 1305–1312. DOI: 10.1016/S0082-0784(06)80394-2.

[65] Jiang L.Y., Han Y., Patnaik P. Characteristics of Volcanic Ash in a Gas Turbine Combustor and Nozzle Guide Vanes. NATO STO-MP-AVT-272, 4/27/2017. Final Report of MP-AVT-272-09.

[66] Brach R.M., Dunn P.F. A mathematical model of the impact and adhesion of microsphers (1992) Aerosol Science and Technology, 16 (1), pp. 51–64. DOI: 10.1080/02786829208959537.

[67] Johnson K.L., Kendall K., Roberts A.D. Surface Energy and the Contact of Elastic Solids (1971) Proceedings of the Royal Society A, 324, pp. 301–313. DOI: 10.1098/rspa.1971.0141.

[68] El-Batsh H. Modeling Particle Deposition on Compressor and Turbine Blade Surfaces. PhD Thesis, Vienna: Vienna University of Technology; 2001.

[69] Ai W. Deposition of Particulate from Coal-Derived Syngas on Gas Turbine Blades Near Film Cooling Holes. PhD Thesis, Provo, Utah: Brigham Young University; 2009. http://scholarsarchive.byu.edu/etd/1916

[70] Bons J.P., Prenter R., Whitaker S. A Simple Physics-Based Model for Particle Rebound and Deposition in Turbomachinery (2017) Journal of Turbomachinery, 139, 081009.

[71] Prenter R., Ameri A., Bons J.P. Computational Simulation of Deposition in a Cooled High-Pressure Turbine Stage With Hot Streaks (2017) Journal of Turbomachinery, 139, 091005.

[72] Forsyth P.R., Gillespie D.R.H., McGilvray M. Development and applications of a coupled particle deposition - Dynamic mesh morphing approach for the numerical simulation of gas turbine flows (2018) Journal of Engineering for Gas Turbines and Power, 140 (2), art. no. 022603. DOI: 10.1115/1.4037825

[73] Agati G., Borello D., Rispoli F., Venturini P. An Innovative Approach to Model Temperature Influence on Particle Deposition in Gas Turbines. ASME Paper 2016:GT2016-57997.

[74] Yu K., Tafti D. Size and temperature dependent deposition model of micro-sized sand particles (2017) Proceedings of the ASME Turbo Expo, 2D-2017. DOI: 10.1115/GT2017-63792

[75] Yu K., Tafti D. Impact model for micrometer-sized sand particles (2016) Powder Technology, 294, pp. 11-21. DOI: 10.1016/j.powtec.2016.02.014

[76] Mysen B.O. Structure and properties of silicate melts (1988) Structure and properties of silicate melts, 368 p. New York: Elsevier.

[77] Mills K.C., Sridhar S. Viscosities of ironmaking and steelmaking slags (1999) Ironmaking and Steelmaking, 26 (4), pp. 262–268. DOI: 10.1179/030192399677121.

[78] Duffy J.A., Ingram M.D. Optical basicity—IV: Influence of electronegativity on the Lewis basicity and solvent properties of molten oxyanion salts and glasses (1975) Journal of Inorganic and Nuclear Chemistry, 37 (5), pp. 1203–1206. DOI: 10.1016/0022-1902(75)80469-6.

[79] Zhang G.-H., Chou K.-C. Simple method for estimating the electrical conductivity of oxide melts with optical basicity (2010) Metallurgical and Materials Transactions B: Process Metallurgy and Materials Processing Science, 41 (1), pp. 131–136. DOI: 10.1007/s11663-009-9298-z.

[80] Giordano D., Russell J.K., Dingwell D.B. Viscosity of magmatic liquids: A model (2008) Earth and Planetary Science Letters, 271 (1-4), pp. 123-134. DOI: 10.1016/j.epsl.2008.03.038.

[81] ASTM D1857-04. Standard test method for fusibility of coal and coke ash. ASTM International, West Conshohocken, PA; 2004.

[82] Yin C., Luo Z., Ni M., Cen K. Predicting coal ash fusion temperature with a back-propagation neural network model (1998) Fuel, 77 (15), pp. 1777–1782. DOI: 10.1016/S0016-2361(98)00077-5.

[83] Bottinga Y., Weill D., Richet P. Density calculations for silicate liquids. I. Revised method for aluminosilicate compositions (1982) Geochimica et Cosmochimica Acta, 46 (6), pp. 909–919. DOI: 10.1016/0016-7037(82)90047-3.

[84] Mills K.C., Keene B.J. Physical properties of BOS slags (1987) International Materials Reviews, 32 (1), pp. 1–120. DOI: 10.1179/095066087790150296.

[85] Ciprian D., Grigore B. Classification and Characterization of Basalts of Branisca and Dobra – Romania, for Capitalization (2009) Recent Advances in Industrial and Manufacturing Technologies, 64–69 (ISBN: 978-1-61804-186-9).

[86] Taylor H.E., Lichte F.E. Chemical Composition of Mount St. Helens Volcanic Ash (1980) Geophysical Research Letters, 7, pp. 949–952.

[87] Guha A. Transport and deposition of particles in turbulent and laminar flow (2008) Annual Review of Fluid Mechanics, 40, pp. 311–341. DOI: 10.1146/annurev.fluid.40.111406.102220

[88] Laycock R.G., Fletcher T.H. Erratum: Time-Dependent Deposition Characteristics of Fine Coal Fly Ash in a Laboratory Gas Turbine Environment [ASME J. Turbomach., 135, 2, (2012) (021003). DOI: 10.1115/1.4006639] (2017) Journal of Turbomachinery, 139 (12), art. no. 127001. DOI: 10.1115/1.4037911

[89] Erratum: “Erratum: ‘Time-Dependent Deposition Characteristics of Fine Coal Fly Ash in a Laboratory Gas Turbine Environment’ [ASME J. Turbomach., 2012, 135(2), p. 021003; DOI:10.1115/1.4006639]” [ASME. J.Turbomach., 2017, 139(12), p. 127001; DOI: 10.1115/1.4037911]

[90] Bell I.H., Wronski J., Quoilin S., Lemort V. Pure and pseudo-pure fluid thermophysical property evaluation and the open-source thermophysical property library CoolProp (2014) Industrial & Engineering Chemistry Research; 53(6), pp. 2498–508. DOI: 10.1021/ie4033999.

[91] Kueppers U., Cimarelli C., Hess K.-U, Taddeucci J., Wadsworth F.B., Dingwell D.B. The thermal stability of Eyjafjallajökull ash versus turbine ingestion test sands (2014) Journal of Applied Volcanology, 3 (1), art. no. 4. DOI: 10.1186/2191-5040-3-4.

[92] Bas M.J.L., Maitre R.W.L., Streckeisen A., Zanettin B. A chemical classification of volcanic rocks based on the total alkali-silica diagram (1986) Journal of Petrology, 27 (3), pp. 745–750. DOI: 10.1093/petrology/27.3.745.

[93] Seetharaman S., Mukai K., Sichen D. Viscosities of slags - An overview (2005) Steel Research International, 76 (4), pp. 267–278. DOI: 10.1002/srin.200506008.

[94] Hsieh P., Kwong K.S., Bennett J. Correlation betweenthe critical viscosity and ash fusion temperatures of coal gasifier ashes (2016) Fuel Processing Technology, 142, pp. 13–26. DOI: 10.1016/j.fuproc.2015.09.019.

[95] ASTM D 2196-15. Standard Test Methods for Rheological Properties of Non-Newtonian Materials by Rotational Viscometer (2015) ASTM International, West Conshohocken, PA.

[96] Mills K.C., Hayashi M., Wang L., Watanabe T. The structure and properties of silicate slags. In: Seetharaman S, McLean A, Guthrie R, editors. Treatise on process metallurgy, Volume 1: Process fundamentals, Amsterdam: Elsevier Ltd; 2014, p. 149–286.

[97] Vargas S., Frandsen F.J., Dam-Johansen K. Rheological properties of high-temperature melts of coal ashes and other silicates (2001) Progress in Energy and Combustion Science, 27 (3), pp. 237–429. DOI: 10.1016/S0360-1285(00)00023-X.

[98] Singh T., Sundararajan G. The erosion behavior of 304 stainless steel at elevated temperatures (1990) Metallurgical Transactions A, 21 (12), pp. 3187–3199. DOI: 10.1007/BF02647314.

[99] Sundararajan G., Roy M. Solid particle erosion behaviour of metallic materials at room and elevated temperatures (1997) Tribology International, 30 (5), pp. 339–359. DOI: 10.1016/S0301-679X(96)00064-3.

[100] Wellman R.G., Nicholls J.R. High temperature erosion-oxidation mechanisms, maps and models (2004) Wear, 256 (9-10), pp. 907–917. DOI: 10.1016/j.wear.2003.04.003.

[101] Shin D., Hamed A. Advanced high temperature erosion tunnel for testing TBC and new turbine blade materials (2016) Proceedings of the ASME Turbo Expo, 6. DOI: 10.1115/GT2016-57922.

[102] Goodwin J.E., Sage W., Tilly G.P. Study of erosion by solid particles (1969) Proceedings of the Institution of Mechanical Engineers, 184, pp. 279–292.

[103] Bitter J.G.A. A study of erosion phenomena part I (1963) Wear, 6 (1), pp. 5–21. DOI: 10.1016/0043-1648(63)90003-6.

[104] Henry C., Minier J.-P. Progress in particle resuspension from rough surfaces by turbulent flows (2014) Progress in Energy and Combustion Science, 45 (C), pp. 1–53. DOI: 10.1016/j.pecs.2014.06.001.

[105] Sacco C., Bowen C., Lundgreen R., Bons J.P., Ruggiero E., Allen J., Bailey J. Dynamic similarity in turbine deposition testing and the role of pressure (2017) Proceedings of the ASME Turbo Expo, 2D-2017. DOI: 10.1115/GT2017-64961.

[106] Zaba T., Lombardi P. Experience in the operation of air filters in gas turbine installations. (1984) American Society of Mechanical Engineers. DOI: 10.1115/84-GT-39.

[107] Tarabrin A.P., Schurovsky V.A., Bodrov A.I., Stalder J.-P. Influence of axial compressor fouling on gas turbine unit performance based on different schemes and with different initial parameters (1998) Proceedings of the ASME Turbo Expo, 4. DOI: 10.1115/98-GT-416.

[108] Syverud E., Brekke O., Bakken L.E. Axial compressor deterioration caused by saltwater ingestion. (2007) Journal of Turbomachinery, 129 (1), pp. 119–126. DOI: 10.1115/1.2219763.

[109] Kurz R., Musgrove G., Brun K. Experimental evaluation of compressor blade fouling. (2017) Journal of Engineering for Gas Turbines and Power, 139 (3), art. no. 032601, DOI: 10.1115/1.4034501.

[110] Vigueras Zuniga M. O., Analysis of Gas Turbine Compressor Fouling and Washing on Line (2007) Ph.D. thesis, Cranfield University, Cranfield, UK.

[111] Carpenter L.K., Crouse Jr. F.W., Halow J.S. Coal-fueled turbines: deposition research. (1985) American Society of Mechanical Engineers, 6 p. DOI: 10.1115/85-GT-213.

APPENDIX A

The NPL model (National Physical Laboratory) is used to calculate the particle viscosity according to the following procedure [77]. The method is based on the optical basicity and the viscosity can be calculated as

$$\ln \mu = \ln A_{\mathrm{NPL}} + \frac{B_{\mathrm{NPL}}}{T} \tag{A1}$$

where the temperature is expressed in [K] and the particle viscosity in [Pa s]. The Optical Basicity (that could be corrected for the cations required for the charge balance of the aluminum oxide) is calculated according to the mol% fraction χ and number of oxygen atoms n in the molecule. The Optical Basicity is used to classify oxides on a scale of acidity, which is referred to the same O^{2-} base. The expression of the Non-Corrected (NC) Optical Basicity Λ^{NC} is the following

$$\Lambda^{\mathrm{NC}} = \frac{\sum \chi_{\mathrm{i}} n_{\mathrm{i}} \Lambda_{\mathrm{i}}}{\sum \chi_{\mathrm{i}} n_{\mathrm{i}}} \tag{A2}$$

where the values of the theoretical Optical Basicity Λ are listed in Table A1. According to the correction proposed by Duffy and Ingram [78], used in [79], the Corrected (C) Optical Basicity Λ^{C} is calculated as

$$\chi_{\mathrm{CaO}} \geq \chi_{\mathrm{Al_2O_3}}$$

$$\Lambda^{\mathrm{C}} = \frac{1\,\Lambda_{\mathrm{CaO}}\left(\chi_{\mathrm{CaO}} - \chi_{\mathrm{Al_2O_3}}\right) + 2\,\Lambda_{\mathrm{SiO_2}}\,\chi_{\mathrm{SiO_2}} + 3\,\Lambda_{\mathrm{Al_2O_3}}\,\chi_{\mathrm{Al_2O_3}} + 1\,\Lambda_{\mathrm{MgO}}\,\chi_{\mathrm{MgO}} + 3\,\Lambda_{\mathrm{Fe_2O_3}}\,\chi_{\mathrm{Fe_2O_3}} + 1\,\Lambda_{\mathrm{Na_2O}}\,\chi_{\mathrm{Na_2O}} + 1\,\Lambda_{\mathrm{K_2O}}\,\chi_{\mathrm{K_2O}} + 2\,\Lambda_{\mathrm{TiO_2}}\,\chi_{\mathrm{TiO_2}}}{1\left(\chi_{\mathrm{CaO}} - \chi_{\mathrm{Al_2O_3}}\right) + 2\,\chi_{\mathrm{SiO_2}} + 3\,\chi_{\mathrm{Al_2O_3}} + 1\,\chi_{\mathrm{MgO}} + 3\,\chi_{\mathrm{Fe_2O_3}} + 1\,\chi_{\mathrm{Na_2O}} + 1\,\chi_{\mathrm{K_2O}} + 2\,\chi_{\mathrm{TiO_2}}} \tag{A3}$$

$$\chi_{\mathrm{CaO}} \leq \chi_{\mathrm{Al_2O_3}} \text{ and } \chi_{\mathrm{CaO}} + \chi_{\mathrm{MgO}} \geq \chi_{\mathrm{Al_2O_3}}$$

$$\Lambda^{\mathrm{C}} = \frac{1\,\Lambda_{\mathrm{MgO}}\,\Lambda_{\mathrm{CaO}}\left(\chi_{\mathrm{CaO}} + \chi_{\mathrm{MgO}} - \chi_{\mathrm{Al_2O_3}}\right) + 2\,\Lambda_{\mathrm{SiO_2}}\,\chi_{\mathrm{SiO_2}} + 3\,\Lambda_{\mathrm{Al_2O_3}}\,\chi_{\mathrm{Al_2O_3}} + 3\,\Lambda_{\mathrm{Fe_2O_3}}\,\chi_{\mathrm{Fe_2O_3}} + 1\,\Lambda_{\mathrm{Na_2O}}\,\chi_{\mathrm{Na_2O}} + 1\,\Lambda_{\mathrm{K_2O}}\,\chi_{\mathrm{K_2O}} + 2\,\Lambda_{\mathrm{TiO_2}}\,\chi_{\mathrm{TiO_2}}}{1\left(\chi_{\mathrm{CaO}} + \chi_{\mathrm{MgO}} - \chi_{\mathrm{Al_2O_3}}\right) + 2\,\chi_{\mathrm{SiO_2}} + 3\,\chi_{\mathrm{Al_2O_3}} + 3\,\chi_{\mathrm{Fe_2O_3}} + 1\,\chi_{\mathrm{Na_2O}} + 1\,\chi_{\mathrm{K_2O}} + 2\,\chi_{\mathrm{TiO_2}}} \tag{A4}$$

Journal of Engineering for Gas Turbines and Power. Received July 29, 2018;
Accepted manuscript posted August 27, 2018. doi:10.1115/1.4041282

If $\chi_{CaO} + \chi_{MgO} \leq \chi_{Al_2O_3}$ the Optical Basicity will not be corrected because, in this case, the Si^{4+} chain or rig is not able to incorporate the Al^{3+} ions and the aluminum oxide behaves as a basic oxide. At this condition, Eq (4) can be applied without correction. The coefficients A and B can be calculated according to the expressions

$$\ln \frac{B_{\mathrm{NPL}}}{1000} = -1.77 + \frac{2.88}{(\Lambda^{\mathrm{C}} \text{or } \Lambda^{\mathrm{NC}})} \tag{A5}$$

$$\ln A_{\mathrm{NPL}} = -232.69(\Lambda^{\mathrm{C}} \text{or } \Lambda^{\mathrm{NC}})^2 + 357.32(\Lambda^{\mathrm{C}} \text{or } \Lambda^{\mathrm{NC}}) - 144.17 \tag{A6}$$

The accuracy of the present method is not reported in the original work [77]. However, by using the data proposed by Duffy and Ingram [78], it is possible to estimate the deviations between the theoretical and the experimental optical basicity values. The data refers to glassy materials and the confidence band is equal to about ± 9 %.

APPENDIX B

The viscosity model proposed by Giordano *et al.* [80] is used to calculated the volcanic ash viscosity according to the following procedure. The former relation is

$$\ln \mu = \ln A_{\mathrm{GRD}} + \frac{B_{\mathrm{GRD}}}{T - C_{\mathrm{GRD}}} \tag{B1}$$

where the temperature is expressed in [K] and the particle viscosity in [Pa s]. The model coefficient A_{GRD} is equal to -4.55 while the coefficients B_{GRD} and C_{GRD} are calculated according to the mol% fraction χ of the constituent oxides

$$\begin{aligned} B_{\mathrm{GRD}} = {} & 159.6(\chi_{\mathrm{SiO_2}} + \chi_{\mathrm{TiO_2}}) - 173.3\chi_{\mathrm{Al_2O_3}} + 72.1\,\chi_{\mathrm{Fe_2O_3}} + 75.7\,\chi_{\mathrm{MgO}} - 39.0\chi_{\mathrm{CaO}} - 84.1\,\chi_{\mathrm{Na_2O}} - 2.43(\chi_{\mathrm{SiO_2}} + \chi_{\mathrm{TiO_2}})(\chi_{\mathrm{Fe_2O_3}} + \chi_{\mathrm{MgO}}) \\ & - 0.91(\chi_{\mathrm{SiO_2}} + \chi_{\mathrm{TiO_2}} + \chi_{\mathrm{Al_2O_3}})(\chi_{\mathrm{Na_2O}} + \chi_{\mathrm{K_2O}}) + 17.6\chi_{\mathrm{Al_2O_3}}(\chi_{\mathrm{Na_2O}} + \chi_{\mathrm{K_2O}}) \end{aligned} \tag{B2}$$

$$\begin{aligned} C_{\mathrm{GRD}} = {} & 2.75\,\chi_{\mathrm{SiO_2}} + 15.7(\chi_{\mathrm{TiO_2}} + \chi_{\mathrm{Al_2O_3}}) + 8.3(\chi_{\mathrm{Fe_2O_3}} + \chi_{\mathrm{MgO}}) + 10.2\chi_{\mathrm{CaO}} - 12.3(\chi_{\mathrm{Na_2O}} + \chi_{\mathrm{K_2O}}) \\ & + 0.3(\chi_{\mathrm{Al_2O_3}} + \chi_{\mathrm{Fe_2O_3}} + \chi_{\mathrm{MgO}} + \chi_{\mathrm{CaO}})(\chi_{\mathrm{Na_2O}} + \chi_{\mathrm{K_2O}}) \end{aligned} \tag{B3}$$

According to Giordano *et al.* [80] the model is calibrated on the composite oxides of the melts as reported here:

- SiO_2 = (41 – 79) wt%;
- CaO = (0 – 26) wt%;
- Al_2O_3 = (0 – 23) wt%;
- Fe_2O_3 = (0 – 12) wt%;
- MgO = (0 – 32) wt%;
- Na_2O = (0 – 11) wt%;
- K_2O = (0.3 – 9) wt%;
- Ti_2O = (0 – 3) wt%.

Journal of Engineering for Gas Turbines and Power. Received July 29, 2018;
Accepted manuscript posted August 27, 2018. doi:10.1115/1.4041282

In Giordano *et al.* [80] a detailed description of the accuracy of the model coefficient A_{GRD} is reported. In addition, the data comparison reported by the Authors showed a root-mean-square-error equal to 0.4 log unit.

APPENDIX C

The model proposed by Yin *et al.* [82] is used for calculating the particle softening temperature. According to the ash composition, the relations used to assess the ash softening temperature are reported as follows:

when the content of SiO_2 is less than or equal to 60 wt%, and the content of Al_2O_3 is greater than 30 wt%

$$T_{soft} = 69.94SiO_2 + 71.01Al_2O_3 + 65.23Fe_2O_3 + 12.16CaO + 68.31MgO + 67.19a - 5485.7 \quad (C1)$$

when the content of SiO_2 is less than or equal to 60 wt%, the content of Al_2O_3 is less than or equal to 30 wt% and the content of Fe_2O_3 is less than or equal to 15 wt%

$$T_{soft} = 92.55SiO_2 + 97.83Al_2O_3 + 84.52Fe_2O_3 + 83.67CaO + 81.04MgO + 91.92a - 7891 \quad (C2)$$

when the content of SiO_2 is less than or equal to 60 wt%, and that of Al_2O_3 is less than or equal to 30 wt%, and that of Fe_2O_3 is greater than 15 wt%

$$T_{soft} = 1531 - 3.01SiO_2 + 5.08Al_2O_3 - 8.02Fe_2O_3 - 9.69CaO - 5.86MgO - 3.99a \quad (C3)$$

and finally, when the content of SiO_2 is greater than 60 wt%

$$T_{soft} = 10.75SiO_2 + 13.03Al_2O_3 - 5.28Fe_2O_3 - 5.88CaO - 10.28MgO - 3.75a + 453 \quad (C4)$$

The constant *a* is defined according to the weight fraction of each component as

$$a = 100 - (SiO_2 + Al_2O_3 + Fe_2O_3 + CaO + MgO) \quad (C5)$$

APPENDIX D

The particle deposition tests collected in Table 1 are reported in this Appendix with the reference of particle Stokes number and particle relaxation time values. For each test, the geometric features of the target are included in the related reference. Particle Stokes number is calculated according to

$$St = \frac{\rho\, d^2\, v}{18\, \mu_g\, L} \quad (D1)$$

where the characteristic target length *L* is affected by inaccuracy as reported below. Particle relaxation time is not affected by these inaccuracies and is calculated according to

$$\tau = \frac{\rho\, d^2}{18\, \mu_g} \quad (D2)$$

In the presence of a certain variability range of particle diameter and temperature, a single average value is assumed as representative of the entire test. The values of the former variables of Stokes number and particle relaxation time are reported in Table D1 as well as the type of target and its shape. In several cases, the geometric characteristics of the target are not reported in detail and for this reason, they are estimated using sketches and figures reported in the correspondent reference with unavoidable inaccuracies. In these cases, the target dimensions reported in Table D1 are marked with a cross.

According to the type of target, the characteristic length L is calculated according to the following rules:

- tests performed on full scale gas turbine (T): a representative chord equal to 50 mm was assumed as characteristic length L for all the tests, excluding the tests called Laki 5 (Shinozaky *et al.* [21]) for which the chord of the first nozzle was estimated using the sketch reported in the reference;
- tests performed on wind tunnels provided with cascade or single blade targets (B): the airfoil chord was assumed as characteristic length L;
- tests performed using a coupon (C): the diameter (if circular) or the hydraulic diameter (if rectangular) of the coupon holder were assumed as characteristic length L;
- tests performed in order to discover particle deposition inside the internal cooling hole (I): the diameter of the circular holes was assumed as characteristic length L.

The dynamic viscosity of the carrier gas is assumed equal to that of pure air at the same temperature and calculated according to CoolProp library [90] for a reference pressure (absolute) equal to 2 bar. In some tests, the carrier gas came from a combustion chamber in which natural gas or other types of fuels (syngas or heavy fuels) were burned.

For these reasons, the Stokes number and particle relaxation time as well as the characteristics length L reported in Table D1 are only useful for an order of magnitude analysis.

List of table captions

List of figure captions

Table 1 – Particle deposition data. Material composition in terms of weight fraction (wt%)

	Authors	Material	*d* [μm]	*ρ* [kg/m^3]	v [m/s]	*T* [K]	TT	Na_2O	K_2O	CaO	MgO	SiO_2	Al_2O_3	TiO_2	Fe_2O_3
2017	Giehl *et al.* [38]	Basalt	5–125	2800	15	1373–1773	C	3.0	0.5	10.2	5.9	52.0	13.0	2.8	12.4
		Andesite	5–125	2600	15	1373–1773	C	3.7	0.7	8.8	5.6	53.9	18.7	1.0	7.4
		Dacite	5–125	2700	15	1373–1773	C	4.4	2.4	3.7	0.8	63.7	13.5	0.8	7.8
		Rhyolite	5–125	2500	15	1373–1773	C	6.4	2.4	2.9	1.0	73.4	11.9	0.9	2.8
	Barker *et al.* [40]	ARD$^+$	10–35	2560	80	1373	C	2.3	3.3	3.8	1.3	72.8	10.8	0.3	5.3
	Boulanger *et al.* [41]	ARD 2$^+$	20–40	2560	70	1273–1373	C	2.3	3.3	3.8	1.3	72.8	10.8	0.3	5.3
	Whitaker *et al.* [52]	ARD 3$^+$	0–10	2560	40	920–1262$^\Delta$	I	2.3	3.3	3.8	1.3	72.8	10.8	0.3	5.3
	Wylie *et al.* [51]	EYJA	4.8–34.9	849	80	1163–1293$^\square$	I	2.0	2.0	4.6	0.0	51.3	10.9	1.4	9.5
		Chaiten VA	4.8–34.9	849	80	1163–1293$^\square$	I	2.9	2.9	1.6	0.0	73.9	14.0	0.2	1.6
2016	Boulanger *et al.* [36]	ARD 4$^+$	20–40	2560	70	1273–1373	C	2.3	3.3	3.8	1.3	72.8	10.8	0.3	5.3
	Whitaker *et al.* [53]	ARD 5$^{+,*}$	0–20	2560	21	866 $^\lozenge$	I	0.0	0.0	3.3	0.0	84.8	9.9	0.0	2.1
	Lundgreen *et al.* [49]	ARD 6$^{+,*}$	0–5	2560	70	1363–1623	B	0.0	0.0	3.0	0.0	85.0	10.0	0.0	2.0
	Dean et al.[37]	Laki$^\times$	5–50	2400	106	1043–1295	C	6.4	0.3	6.3	8.3	52.6	18.8	1.3	6.1
		Hekla$^{2\times}$	5–50	1500	106	1043–1295	C	7.3	1.2	2.0	1.4	67.4	18.1	0.0	2.6
		Eldgja$^{3\times}$	5–50	1900	106	1043–1295	C	6.9	0.3	6.2	7.1	50.3	19.7	2.4	7.3
		Askja$^{4\times}$	5–50	1400	106	1043–1295	C	5.6	1.5	1.7	1.8	71.9	15.5	0.0	2.0
	Laycock and Fletcher [35]	JBPS A	4	2330	200	1523–1673	C	2.5	0.9	5.1	1.6	63.6	17.3	1.1	4.2
	Taltavull *et al.* [39]	Laki 2$^{5\times}$	10–70	2400	91	1043	C	1.2	0.1	7.8	3.1	47.2	11.6	3.7	25.2
		Laki 3$^{5\times}$	10–70	2400	106	1160	C	1.2	0.1	7.8	3.1	47.2	11.6	3.7	25.2
		Laki 4$^{5\times}$	10–70	2400	127	1295	C	1.2	0.1	7.8	3.1	47.2	11.6	3.7	25.2
'15	Whitaker *et al.* [48]	JBPS B	4.63; 6.48	2320	70	1353	B	3.7	1.6	9.4	1.7	49.9	11.5	3.0	14.5
'14	Prenter *et al.* [47]	JBPS B	6.48	2320	70	1353	B	3.7	1.6	9.4	1.7	49.9	11.5	3.0	14.5
2013	Casaday *et al.* [46]	JBPS B 2	11.6	2320	79	1366	B	3.7	1.6	9.4	1.7	49.9	11.5	3.0	14.5
	Laycock and Fletcher [34], [88], [89]	JBPP **	3; 13	1980	200	1523	C	3.9	1.7	9.9	1.8	52.4	12.1	3.1	15.2
	Shinozaki *et al.* [21]	Laki 5	20–100	2400	365	1343	T	1.2	0.1	7.8	3.1	47.2	11.6	3.7	25.2
2	Webb *et al.* [45]	Lignite	12.5	2818	70	1314–1371	B	0.8	1.0	31.7	3.6	32.8	14.2	2.6	9.8

		Bituminous	14.1	1980	70	1339–1366	B	0.3	2.0	2.3	0.6	25.3	11.0	1.9	52.7
		PRB	18.3	2989	70	1315–1385	B	1.8	0.5	42.2	6.9	22.1	10.5	2.2	6.1
		JBPS B 3	12.5	2320	70	1317–1343	B	3.7	1.6	9.4	1.7	49.9	11.5	3.0	14.5
	Ai *et al.* [33]	**Coal(bit.)**	13.4	1980	170	1456	C	6.9	2.6	8.7	3.6	47.4	17.8	1.6	6.4
	Ai *et al.* [32]	**Coal(bit.) 2**	16	1980	180	1453	C	6.9	2.6	8.7	3.6	47.4	17.8	1.6	6.4
'11	**Ai *et al.* [31]**	**Coal(bit.) 3**	4, 13.4	1980	170	1453	C	6.9	2.6	8.7	3.6	47.4	17.8	1.6	6.4
'10	**Smith *et al.* [44]**	**Bituminous mean14**	14	1980	70	1181–1272	B	0.0	2.5	2.9	0.0	32.9	20.3	0.0	40.6
2008	**Crosby *et al.* [30]**	**Coal(bit.) 4**	3.1–16	1980	170	1133–1456	C	6.9	2.6	8.7	3.6	47.4	17.8	1.6	6.4
		Petcoke	6.3	2900	170	1133–1456	C	4.3	2.5	7.5	2.2	38.3	14.5	0.8	22.9
	Wammack *et al.* [29]	**BYU SEM**	16	2500	220	1423	C	0.0	7.3	13.7	0.0	60.2	4.5	0.0	10.7
2007	**Bons *et al.* [28]**	**Coal (bit.) 5**	13.3	1980	200	1423	C	6.9	2.6	8.7	3.6	47.4	17.8	1.6	6.4
		Petcoke 2	33.0	2900	200	1423	C	4.3	2.5	7.5	2.2	38.3	14.5	0.8	22.9
		Straw	17.6	1680	200	1423	C	1.7	23.4	7.8	2.5	48.4	1.8	0.0	5.0
		Sawdust	19.7	960	200	1423	C	5.9	10.7	42.9	12.4	11.6	5.1	1.3	1.0
'05	**Jensen *et al.* [27]**	**BYU SEM**	16	2500	220	1423	C	0.0	7.3	13.7	0.0	60.2	4.5	0.0	10.7
'96	**Dunn *et al.* [20]**	**St Helens Twin Mountain**	23, 73	2700, 2730	100	1283–1558	T	4.5, 0.5	1.6, 4.2	4.5, 10.6	1.6, 1.5	63.2, 50.3	16.4, 13.2	0.6, 1.9	4.1, 15.3
'93	**Kim *et al.* [19]**	**St Helens 2**	23	2700	100	1394–1494	T	4.5	1.6	4.5	1.6	63.2	16.4	0.6	4.1
1992	**Richards *et al.* [25]**	**Arkwright**	0–40	1980	300	1373	C	0.9	1.2	5.8	1.3	48.1	25.1	1.3	11.0
		Blue Gem	0–40	1980	300	1373	C	1.5	0.5	7.0	2.5	16.9	22.8	2.0	29.6
		Arkwright 2	0–20	1980	300	1573	C	0.9	1.2	5.8	1.3	48.1	25.1	1.3	11.0
		Blue Gem 2	0–20	1980	300	1573	C	1.5	0.5	7.0	2.5	16.9	22.8	2.0	29.6
1990	**Anderson *et al.* [24]**	**Arkwright**	0–40	1980	300	1373	C	0.9	1.2	5.8	1.3	48.1	25.1	1.3	11.0
		Blue Gem	0–40	1980	300	1373	C	1.5	0.5	7.0	2.5	16.9	22.8	2.0	29.6
		Arkwright 2	0–20	1980	300	1573	C	0.9	1.2	5.8	1.3	48.1	25.1	1.3	11.0
		Blue Gem 2	0–20	1980	300	1573	C	1.5	0.5	7.0	2.5	16.9	22.8	2.0	29.6
	Wenglarz and Fox [13], [14]	**Ash-fuel 1**	10.2	1900	150	1253–1373	C	0.6	1.2	3.8	0.0	12.0	14.2	0.8	20.4
		Ash-fuel 2	8.5	1900	150	1253–1373	C	0.7	1.0	3.4	0.0	11.5	13.9	0.8	21.9
		Ash-fuel 3	14.5	1900	150	1253–1373	C	1.0	0.9	4.7	0.1	7.5	10.9	1.0	23.1
1989	**Ahluwalia *et al.* [61]**	**Ash-fuel 1**	10.2	1900	150	1253–1373	C	0.6	1.2	3.8	0.0	12.0	14.2	0.8	20.4
		Ash-fuel 2	8.5	1900	150	1253–1373	C	0.7	1.0	3.4	0.0	11.5	13.9	0.8	21.9
		Ash-fuel 3	14.5	1900	150	1253–1373	C	1.0	0.9	4.7	0.1	7.5	10.9	1.0	23.1

1988	**Ross *et al.* [23]**	**Arkwright3**	20	1980	100	1400–1500▼	C	0.9	1.2	5.8	1.3	48.1	25.1	1.3	11.0
		Kentucky	20	1980	100	1400–1500▼	C	9.5	0.3	1.3	0.6	25.5	15.9	7.8	32.4
		Spring Montana	20	1980	100	1400–1500▼	C	13.1	0.1	26.5	6.5	18.6	13.5	1.3	4.7
		North Dakota	20	1980	100	1400–1500▼	C	8.3	0.3	22.9	6.7	20.1	11.2	0.5	13.2
1987	**Spiro *et al.* [12]**	**AMAX**	0–15	1900	100	1366▶	B	6.7	5.8	3.2	0.0	17.9	11.5	2.9	37.6
		Otisca coal	0–11.5	1900	100	1366▶	B	0.5	0.5	11.6	0.0	16.1	23.2	1.1	28.2
	Wenglarz [10]	**Ash-fuel 1**	10.2	1900	150	1253–1373	C	0.6	1.2	3.8	0.0	12.0	14.2	0.8	20.4
		Ash-fuel 2	8.5	1900	150	1253–1373	C	0.7	1.0	3.4	0.0	11.5	13.9	0.8	21.9
		Ash-fuel 3	14.5	1900	150	1253–1373	C	1.0	0.9	4.7	0.1	7.5	10.9	1.0	23.1
	Kimura *et al.* [11]	**Otisca coal**	0–11.5	1900	100	1366	B	0.5	0.5	11.6	0.0	16.1	23.2	1.1	28.2
1984	**Raj and Moskowitz [43]**	**Coal**	0–6	1900	244	1144–1422	B	2.2	2.8	0.3	1.1	28.9	29.4	1.7	25.6
	Anderson *et al.* [22]	**Pittsburg**	15	2500	53	1590	C	0.9	1.2	5.8	1.2	47.9	25.0	1.3	10.9
		Pittsburg 2	15	2500	149	1590	C	0.9	1.2	5.8	1.2	47.9	25.0	1.3	10.9
		Pittsburg 3	15	2500	215	1590	C	0.9	1.2	5.8	1.2	47.9	25.0	1.3	10.9
'83	**Raj [42]**	**Coal 2**	0 – 6	1900	244	1700–1922	B	2.2	2.8	0.3	1.1	28.9	29.4	1.7	25.6

[+] The particle diameters used in these tests could be different from the standard ones reported in the ISO 12103-1 (A1, A2 A3 and A4) due to filtration, sieving and processes applied by the Authors

* ARD 5 and ARD 6 have different chemical compositions with respect to ARD, ARD 2, ARD 3 and ARD 4

[Δ] Temperature values refer to the surface wall temperature. Gas temperature was set equal to 866 K

[□] Temperature values refer to the surface wall temperature. Gas temperature was set in the range (800 – 900) K

[◊] Temperature values was set in the range (700 – 866) K but particle deposition was founded for the highest temperature value (866 K)

[×] The chemical composition in terms of oxide weight fraction was derived starting from the element count % reported in [37] (Si 17.5 %, Al 7.1 %, Na 3.4 %, Ca 3.2 %, Mg 3.6 %, Ti 0.6 %, K 0.2 % and Fe 3.4 %)

[2×] The chemical composition in terms of oxide weight fraction was derived starting from the element count % reported in [37] (Si 21.4 %, Al 6.5 %, Na 3.7 %, Ca 1.0 %, Mg 0.6 %, Ti 0.0 %, K 0.7 % and Fe 1.4 %)

[3×] The chemical composition in terms of oxide weight fraction was derived starting from the element count % reported in [37] (Si 16.0 %, Al 7.1 %, Na 3.5 %, Ca 3.0 %, Mg 2.9 %, Ti 1.0 %, K 0.2 % and Fe 3.9 %)

[4×] The chemical composition in terms of oxide weight fraction was derived starting from the element count % reported in [37] (Si 23.6 %, Al 5.8 %, Na 2.9 %, Ca 0.9 %, Mg 0.8 %, Ti 0.0 %, K 0.9 % and Fe 1.1 %)

[5×] The chemical composition in terms of oxide weight fraction was derived starting from the element count % reported in [21] and [39] and it is different from the Laki composition reported in [37] (Si 24.0 %, Al 6.7 %, Na 1.0 %, Ca 6.1 %, Mg 2.0 %, Ti 2.4 %, K 0.1 % and Fe 21.3 %)

** The details about the composition are based on the second erratum [89]. This composition corrects the previous incorrect compositions reported in the former paper [34] and in the correspondent erratum [88]. The powder belongs to the Jim Bridger Power Plant as well as the tests named JBPS A, JBPS B, 1, 2 and 3 but has a slightly different chemical composition. The weight percent values reported in the table were calculated starting from the following molar percentages (SiO_2 60.2 %, Al_2O_3 8.17 %, Na_2O 4.3 %, CaO 12.2 %, MgO 3.1 %, TiO_2 2.7 %, K_2O 1.2 % and Fe_2O_3 6.6 %)

▼ Temperature range obtained as a function of the distance between nozzle and target.

► Maximum firing temperature

Table 2 – Particle softening temperature

Material	T_{soft} **[K]**	**Material**	T_{soft} **[K]**
Basalt	1170	Coal (bitum.), 2, 3, 4, 5	1278
Andesite	1257	Bituminous mean14	1030
Dacite	1284	Petcoke, 2	1162
Rhyolite	1387	BYU SEM	1071
ARD, 2, 3, 4	1337	Straw	1213
EYJA	1305	Sawdust	842
Chaiten VA	1446	St Helens, 2	1323
ARD 5	1465	Twin Mountain	1176
ARD 6	1471	Arkwright, 2, 3	1337
Laki	1258	Blue Gem, 2	1191
Hekla	1394	Ash-fuel 1	1169
Eldgja	1341	Ash-fuel 2	1162
Askja	1161	Ash-fuel 3	1118
JBPS A	1329	Kentucky	1162
Laki 2, 3, 4, 5	1132	Spring Montana	1068
JBPS B, 2, 3	1197	North Dakota	1021
JBPP	1172	AMAX	1084
Lignite	1032	Otisca coal	1179
Bituminous	1030	Coal, 2	1320
PRB	909	Pittsburgh, 2, 3	1337

Journal of Engineering for Gas Turbines and Power. Received July 29, 2018;
Accepted manuscript posted August 27, 2018. doi:10.1115/1.4041282

Table 3 – Particle erosion/rebound data. Material composition in terms of weight fraction (wt%)

	Authors	Material	d [µm]	ρ [kg/m^3]	v [m/s]	T [K]	T_{soft} [K]	TT	Na_2O	K_2O	CaO	MgO	SiO_2	Al_2O_3	TiO_2	Fe_2O_3
'13	Shinozaki *et al.* [21]	Laki 6	20–100	2400	115	983	1258	T	1.2	0.1	7.8	3.1	47.2	11.6	3.7	25.2
'92	Tabakoff *et al.* [57]	Coal ash	15	2900	366	800 – 1089	1288	C	0.0	0.0	0.0	0.9	48.1	21.2	0.0	20.1
'84	Tabakoff [56]	CG&E	38.4	2900	240	422 – 922	1288	C	0.0	0.0	0.0	0.9	48.1	21.2	0.0	20.1
'81	Kotwal and Tabakoff [55]	CG&E 2	38.4	2900	228	756	1288	C	0.0	0.0	0.0	0.9	48.1	21.2	0.0	20.1
		Kingston	15, 28	2900	228	756	1408	C	0.2	2.1	1.3	1.0	54.4	28.6	0.5	10.1

Journal of Engineering for Gas Turbines and Power. Received July 29, 2018;
Accepted manuscript posted August 27, 2018. doi:10.1115/1.4041282

Table 4 – Particle splashing data. Material composition in terms of weight fraction (wt%)

	Authors	Material	d [µm]	ρ [kg/m^3]	v [m/s]	T [K]	T_{soft} [K]	TT	Na_2O	K_2O	CaO	MgO	SiO_2	Al_2O_3	TiO_2	Fe_2O_3
2016	Dean *et al.* [37]	Laki 7	6500	2400	106	1473	1161	C	6.4	0.3	6.3	8.3	52.6	18.8	1.3	6.1
		Hekla 2	6500	1500	106	1473	1290	C	7.3	1.2	2.0	1.4	67.4	18.1	0.0	2.6
		Eldgja 2	6500	1900	106	1473	1161	C	6.9	0.3	6.2	7.1	50.3	19.7	2.4	7.3

Journal of Engineering for Gas Turbines and Power. Received July 29, 2018;
Accepted manuscript posted August 27, 2018. doi:10.1115/1.4041282

Table A1 – Values of the theoretical basicity Λ

K_2O	Na_2O	CaO	MgO	Al_2O_3	TiO_2	SiO_2	Fe_2O_3
1.40	1.15	1.00	0.78	0.60	0.61	0.48	0.75

Table D1 – Dynamic characteristics of the impacts: Stokes number and particle relaxation time

	Authors	Material	d [μm]	ρ [kg/m^3]	v [m/s]	T [K]	$\mu\times10^5$ [Pa s]	TT	Target	L [m]	St	τ [s]
2017	Giehl *et al.* [38]	Basalt	65.0	2800	15	1573	5.81	C	(20 × 30) mm $^+$	0.024	7.07	1.1e-2
		Andesite	65.0	2600	15	1573	5.81	C	(20 × 30) mm $^+$	0.024	6.56	1.1e-2
		Dacite	65.0	2700	15	1573	5.81	C	(20 × 30) mm $^+$	0.024	6.82	1.1e-2
		Rhyolite	65.0	2500	15	1573	5.81	C	(20 × 30) mm $^+$	0.024	6.31	1.0e-2
	Barker *et al.* [40]	ARD	22.5	2560	80	1373	5.32	C	(63.5 × 38.1) mm	0.048	2.27	1.4e-3
	Boulanger *et al.* [41]	ARD 2	30.0	2560	70	1323	5.19	C	(63.5 × 38.1) mm	0.048	3.62	2.5e-3
	Whitaker *et al.* [52]	ARD 3	5.0	2560	40	1091	4.58	I	0.635 mm	0.001	4.89	7.8e-5
	Wylie *et al.* [51]	EYJA	19.9	849	80	1228	4.95	I	0.675 mm (averaged among 3 tests)	0.001	44.52	3.8e-4
		Chaiten VA	19.9	849	80	1228	4.95	I	0.675 mm (averaged among 3 tests)	0.001	44.52	3.8e-4
2016	Boulanger *et al.* [36]	ARD 4	30.0	2560	70	1323	5.19	C	(63.5 × 38.1) mm	0.048	3.62	2.5e-3
	Whitaker *et al.* [53]	ARD 5	10.0	2560	21	866	3.94	I	0.635 mm	0.001	11.94	3.6e-4
	Lundgreen *et al.* [49]	ARD 6	2.5	2560	70	1493	5.62	B	42 mm $^+$	0.042	0.03	1.6e-5
	Dean *et al.* [37]	Laki	27.5	2400	106	1169	4.79	C	(50 × 30) mm	0.038	5.95	2.1e-3
		Hekla	27.5	1500	106	1169	4.79	C	(50 × 30) mm	0.038	3.72	1.3e-3
		Eldgja	27.5	1900	106	1169	4.79	C	(50 × 30) mm	0.038	4.71	1.7e-3
		Askja	27.5	1400	106	1169	4.79	C	(50 × 30) mm	0.038	3.47	1.2e-3
	Laycock and Fletcher [35]	JBPS A	4.0	2330	200	1598	5.87	C	(75 × 75) mm $^+$	0.075	0.09	3.5e-5

		Laki 2	40.0	2400	91	1043	4.45	C	(50 × 30) mm +	0.038	11.64	4.8e-3
	Taltavull *et al.* [39]	**Laki 3**	40.0	2400	106	1160	4.77	C	(50 × 30) mm +	0.038	12.65	4.5e-3
		Laki 4	40.0	2400	127	1265	5.12	C	(50 × 30) mm +	0.038	14.11	4.2e-3
'15	**Whitaker *et al.* [48]**	**JBPS B**	5.6	2320	70	1353	5.27	B	42 mm +	0.042	0.13	7.5e-5
'14	**Prenter *et al.* [47]**	**JBPS B**	6.5	2320	70	1353	5.27	B	42 mm +	0.042	0.17	1.0e-4
2013	**Casaday *et al.* [46]**	**JBPS B 2**	11.6	2320	79	1366	5.30	B	42 mm +	0.042	0.62	3.3e-4
	Laycock and Fletcher [34], [88], Errore. L'origine riferimento non è stata trovata.	**JBPP**	8.0	1980	200	1523	5.69	C	(75 × 75) mm +	0.075	0.33	1.2e-4
	Shinozaki *et al.* [21]	**Laki 5**	60	2400	365	1343	5.24	T	15 mm +	0.015	223	9.2e-3
2012	**Webb *et al.* [45]**	**Lignite**	12.5	2818	70	1343	5.24	B	42 mm +	0.042	0.78	4.7e-4
		Bituminous	14.1	1980	70	1353	5.27	B	42 mm +	0.042	0.69	4.2e-4
		PRB	18.3	2989	70	1350	5.26	B	42 mm +	0.042	1.76	1.1e-3
		JBPS B 3	12.5	2320	70	1330	5.21	B	42 mm +	0.042	0.64	3.9e-4
	Ai *et al.* [33]	**Coal(bit.)**	13.4	1980	170	1456	5.53	C	31.8 mm	0.032	1.91	3.6e-4
	Ai *et al.* [32]	**Coal(bit.) 2**	16.0	1980	180	1453	5.52	C	31.8 mm	0.032	2.89	5.1e-4
'11	**Ai *et al.* [31]**	**Coal(bit.) 3**	9.0	1980	170	1453	5.52	C	31.8 mm	0.032	0.86	1.6e-4
'10	**Smith *et al.* [44]**	**Bituminous mean14**	14.0	1980	70	1227	4.94	B	42 mm +	0.042	0.73	4.4e-4
2008	**Crosby *et al.* [30]**	**Coal(bit.) 4**	9.6	1980	170	1295	5.12	C	31.8 mm	0.032	1.05	2.0e-4

		Petcoke	6.3	2900	170	1295	5.12	C	31.8 mm	0.032	0.67	1.2e-4
	Wammack *et al.* [29]	**BYU SEM**	16.0	2500	220	1423	5.44	C	31.8 mm	0.032	4.52	6.5e-4
2007	**Bons *et al.* [28]**	**Coal (bit.) 5**	13.3	1980	200	1423	5.44	C	31.8 mm	0.032	2.47	3.6e-4
		Petcoke 2	33.0	2900	200	1423	5.44	C	31.8 mm	0.032	22.27	3.2e-3
		Straw	17.6	1680	200	1423	5.44	C	31.8 mm	0.032	3.34	5.3e-4
		Sawdust	19.7	960	200	1423	5.44	C	31.8 mm	0.032	2.39	3.8e-4
'05	**Jensen *et al.* [27]**	**BYU SEM**	16.0	2500	220	1423	5.44	C	31.8 mm	0.032	4.52	6.5e-4
'96	**Dunn *et al.* [20]**	**St Helens**	23.0	2700	100	1421	5.44	T	50 mm $^{++}$	0.050	2.92	1.5e-3
		Twin Mountain	73.0	2730	100	1421	5.44	T	50 mm $^{++}$	0.050	29.73	1.5e-2
'93	**Kim *et al.* [19]**	**St Helens 2**	23.0	2700	100	1444	5.50	T	50 mm $^{++}$	0.050	2.89	1.4e-3
1992	**Richards *et al.* [25]**	**Arkwright**	20.0	1980	300	1373	5.32	C	12.7 mm	0.013	19.54	8.3e-4
		Blue Gem	20.0	1980	300	1373	5.32	C	12.7 mm	0.013	19.54	8.3e-4
		Arkwright 2	10.0	1980	300	1573	5.81	C	12.7 mm	0.013	4.47	1.9e-4
		Blue Gem 2	10.0	1980	300	1573	5.81	C	12.7 mm	0.013	4.47	1.9e-4
1990	**Anderson *et al.* [24]**	**Arkwright**	20.0	1980	300	1373	5.32	C	12.7 mm	0.013	19.54	8.3e-4
		Blue Gem	20.0	1980	300	1373	5.32	C	12.7 mm	0.013	19.54	8.3e-4
		Arkwright 2	10.0	1980	300	1573	5.81	C	12.7 mm	0.013	4.47	1.9e-4
		Blue Gem 2	10.0	1980	300	1573	5.81	C	12.7 mm	0.013	4.47	1.9e-4

Journal of Engineering for Gas Turbines and Power. Received July 29, 2018;
Accepted manuscript posted August 27, 2018. doi:10.1115/1.4041282

		Ash-fuel 1	10.2	1900	150	1313	5.17	C	(20 × 150) mm [+]	0.035	0.90	2.1e-4
	Wenglarz and Fox [13], [14]	**Ash-fuel 2**	8.5	1900	150	1313	5.17	C	(20 × 150) mm [+]	0.035	0.63	1.5e-4
		Ash-fuel 3	14.5	1900	150	1313	5.17	C	(20 × 150) mm [+]	0.035	1.83	4.3e-4
1989		**Ash-fuel 1**	10.2	1900	150	1313	5.17	C	(20 × 150) mm [+]	0.035	0.90	2.1e-4
	Ahluwalia *et al.* [61]	**Ash-fuel 2**	8.5	1900	150	1313	5.17	C	(20 × 150) mm [+]	0.035	0.63	1.5e-4
		Ash-fuel 3	14.5	1900	150	1313	5.17	C	(20 × 150) mm [+]	0.035	1.83	4.3e-4
1988	**Ross *et al.* [23]**	**Arkwright3**	20.0	1980	100	1450	5.51	C	8 mm	0.008	9.98	8.0e-4
		Kentucky Spring	20.0	1980	100	1450	5.51	C	8 mm	0.008	9.98	8.0e-4
		Montana North Dakota	20.0	1980	100	1450	5.51	C	8 mm	0.008	9.98	8.0e-4
1987	**Spiro *et al.* [12]**	**AMAX**	7.5	1900	100	1366	5.30	B	50 mm [++]	0.050	0.22	1.1e-4
		Otisca coal	5.8	1900	100	1366	5.30	B	50 mm [++]	0.050	0.13	6.6e-5
	Wenglarz [10]	**Ash-fuel 1**	10.2	1900	150	1313	5.17	C	(20 × 150) mm [+]	0.035	0.90	2.1e-4
		Ash-fuel 2	8.5	1900	150	1313	5.17	C	(20 × 150) mm [+]	0.035	0.63	1.5e-4
		Ash-fuel 3	14.5	1900	150	1313	5.17	C	(20 × 150) mm [+]	0.035	1.83	4.3e-4
	Kimura *et al.* [11]	**Otisca coal**	5.8	1900	100	1366	5.30	B	50 mm [++]	0.050	0.13	6.6e-5
1984	**Raj and Moskowitz [43]**	**Coal**	3.0	1900	244	1283	5.09	B	16 mm	0.016	0.28	1.9e-4
	Anderson *et al.* [20]	**Pittsburg**	15.0	2500	53	1590	5.85	C	8 mm	0.008	3.54	5.3e-4

		Pittsburg 2	15.0	2500	149	1590	5.85	C	8 mm	0.008	9.95	5.3e-4
		Pittsburg 3	15.0	2500	215	1590	5.85	C	8 mm	0.008	14.35	5.3e-4
'83	**Raj [42]**	**Coal 2**	3.0	1900	244	1811	6.37	B	50 mm [++]	0.050	0.07	1.5e-5

[+] Estimated by sketches and pictures

[++] Assumed as a representative chord of the first turbine section nozzle

Journal of Engineering for Gas Turbines and Power. Received July 29, 2018;
Accepted manuscript posted August 27, 2018. doi:10.1115/1.4041282

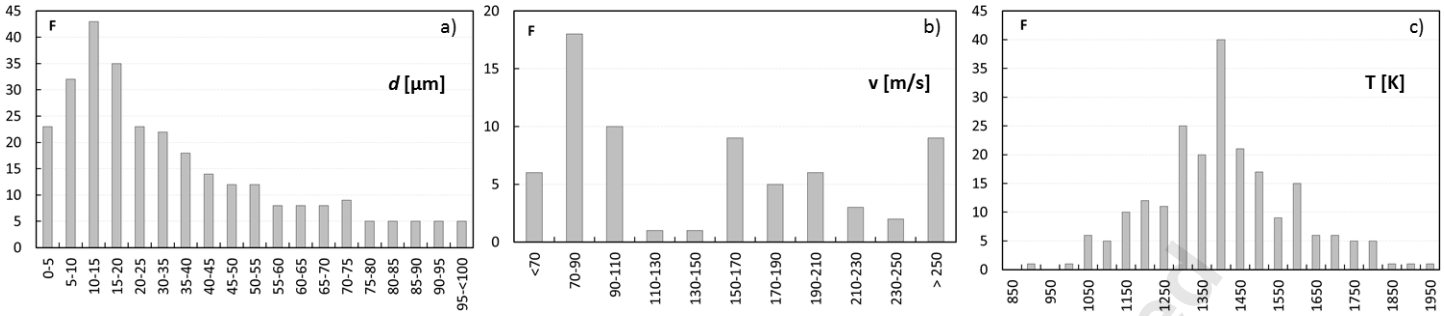

Figure_1_GTP-18-1525

Journal of Engineering for Gas Turbines and Power. Received July 29, 2018;
Accepted manuscript posted August 27, 2018. doi:10.1115/1.4041282

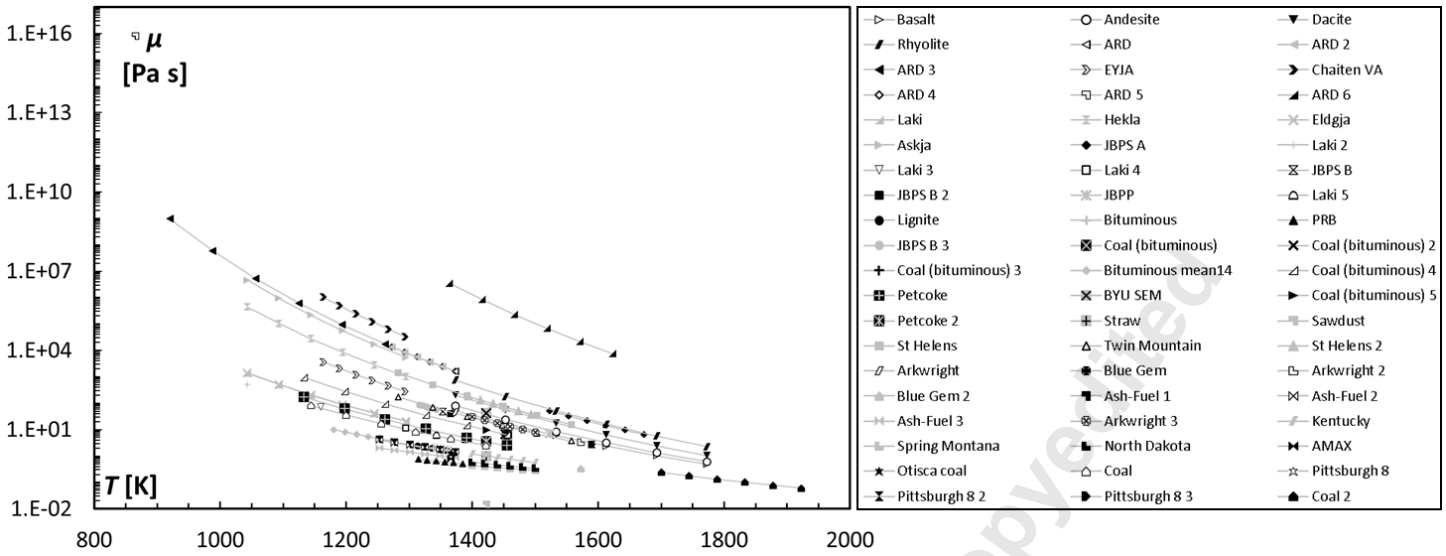

Figure_2_GTP-18-1525

Journal of Engineering for Gas Turbines and Power. Received July 29, 2018;
Accepted manuscript posted August 27, 2018. doi:10.1115/1.4041282

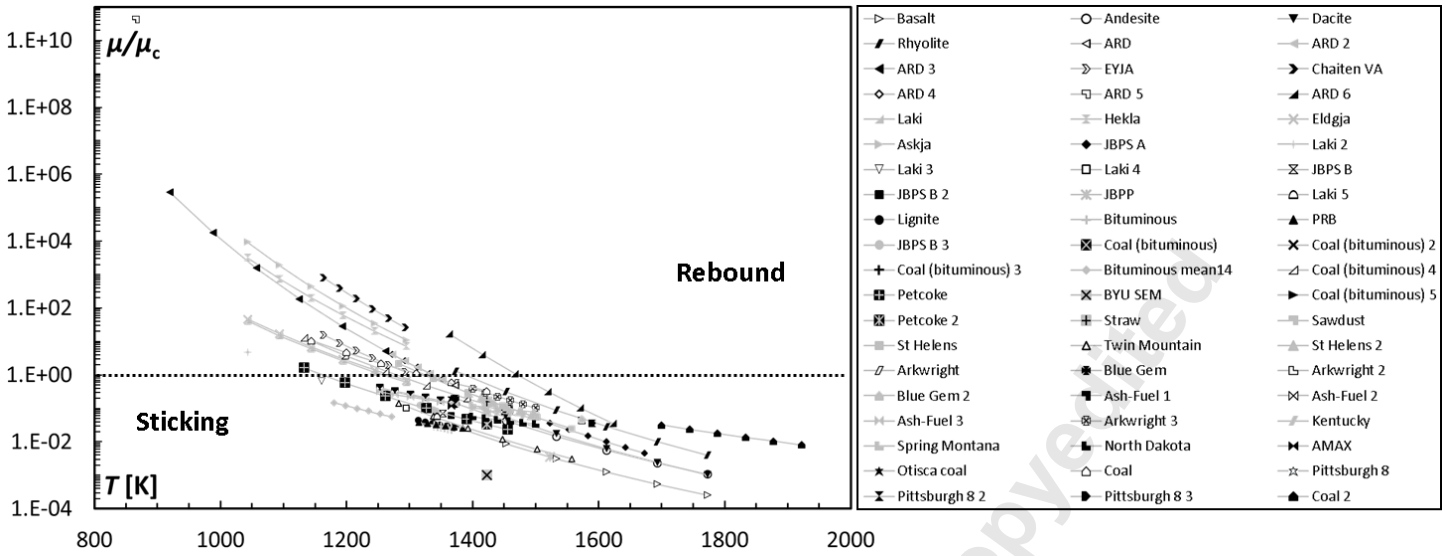

Figure_3_GTP-18-1525

Journal of Engineering for Gas Turbines and Power. Received July 29, 2018;
Accepted manuscript posted August 27, 2018. doi:10.1115/1.4041282

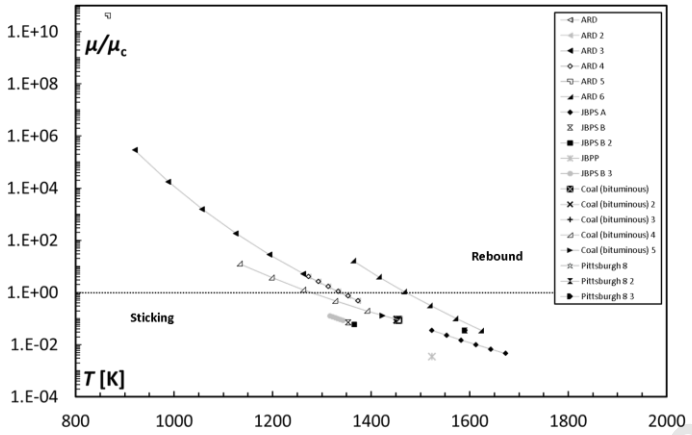

Figure_4_GTP-18-1525

Journal of Engineering for Gas Turbines and Power. Received July 29, 2018;
Accepted manuscript posted August 27, 2018. doi:10.1115/1.4041282

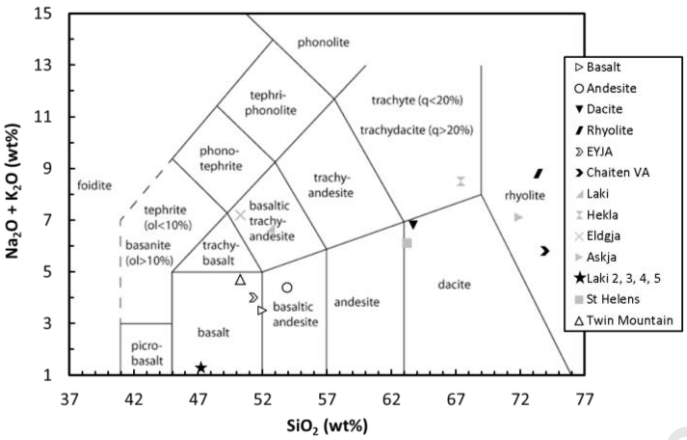

Figure_5_GTP-18-1525

Journal of Engineering for Gas Turbines and Power. Received July 29, 2018;
Accepted manuscript posted August 27, 2018. doi:10.1115/1.4041282

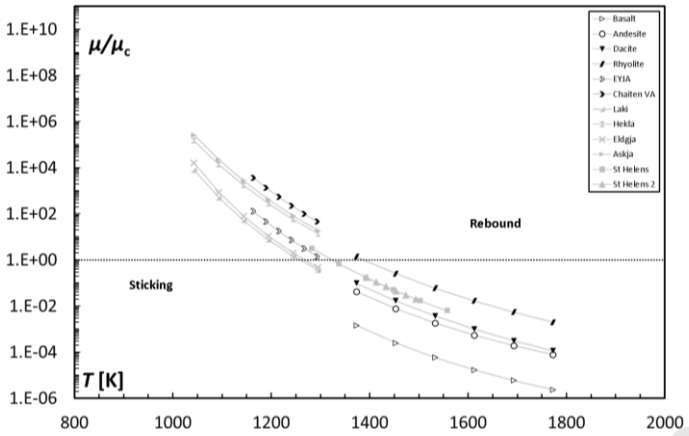

Figure_6_ GTP-18-1525

Journal of Engineering for Gas Turbines and Power. Received July 29, 2018;
Accepted manuscript posted August 27, 2018. doi:10.1115/1.4041282

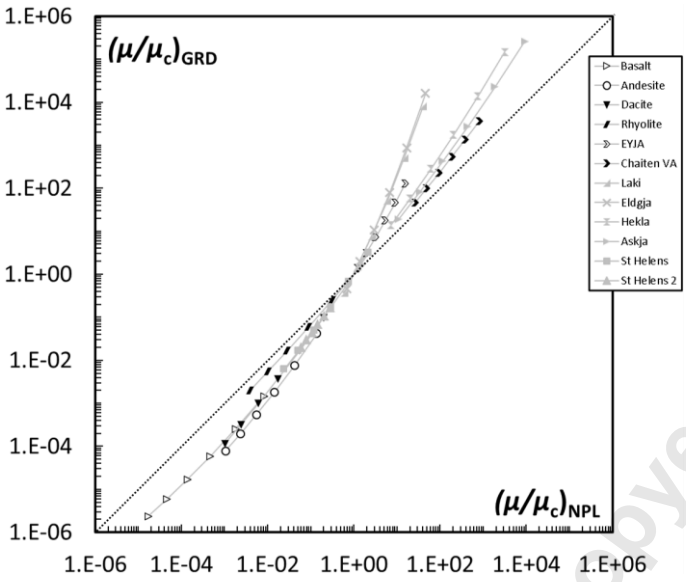

Figure_7_GTP-18-1525

Journal of Engineering for Gas Turbines and Power. Received July 29, 2018;
Accepted manuscript posted August 27, 2018. doi:10.1115/1.4041282

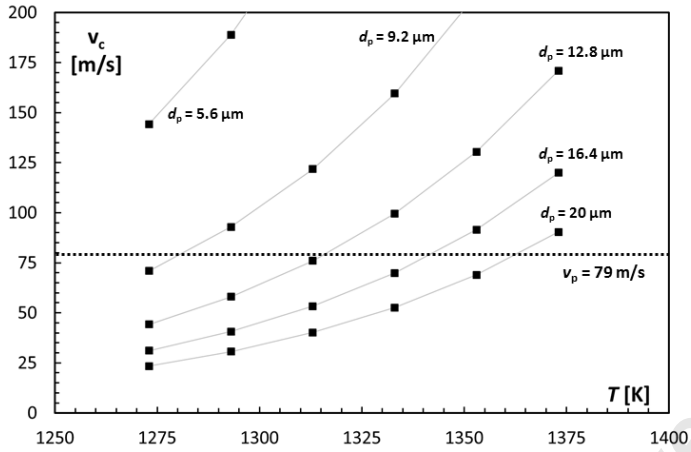

Figure_8_GTP-18-1525

Journal of Engineering for Gas Turbines and Power. Received July 29, 2018;
Accepted manuscript posted August 27, 2018. doi:10.1115/1.4041282

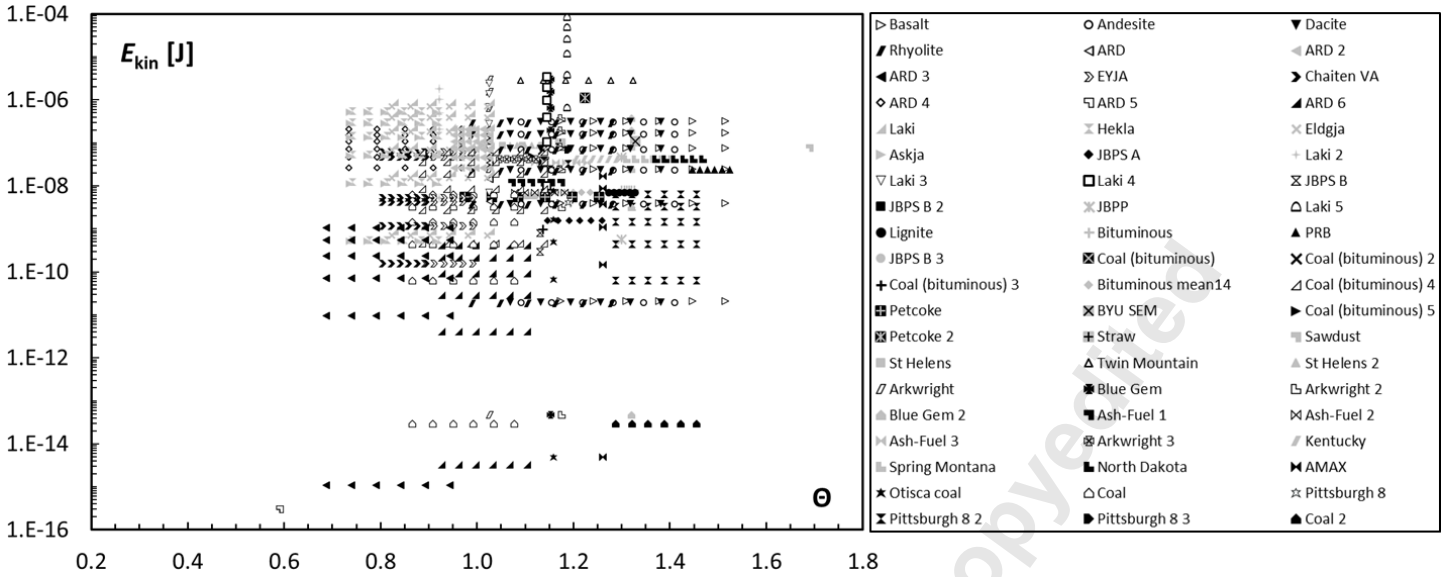

Figure_9_GTP-18-1525

Journal of Engineering for Gas Turbines and Power. Received July 29, 2018;
Accepted manuscript posted August 27, 2018. doi:10.1115/1.4041282

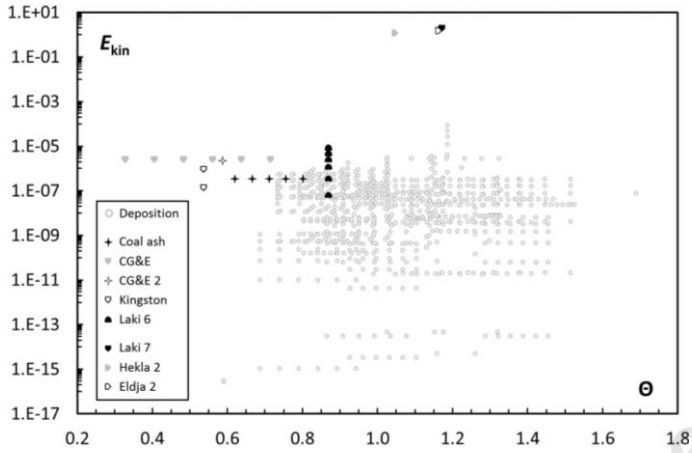

Figure_10_GTP-18-1525

Journal of Engineering for Gas Turbines and Power. Received July 29, 2018;
Accepted manuscript posted August 27, 2018. doi:10.1115/1.4041282

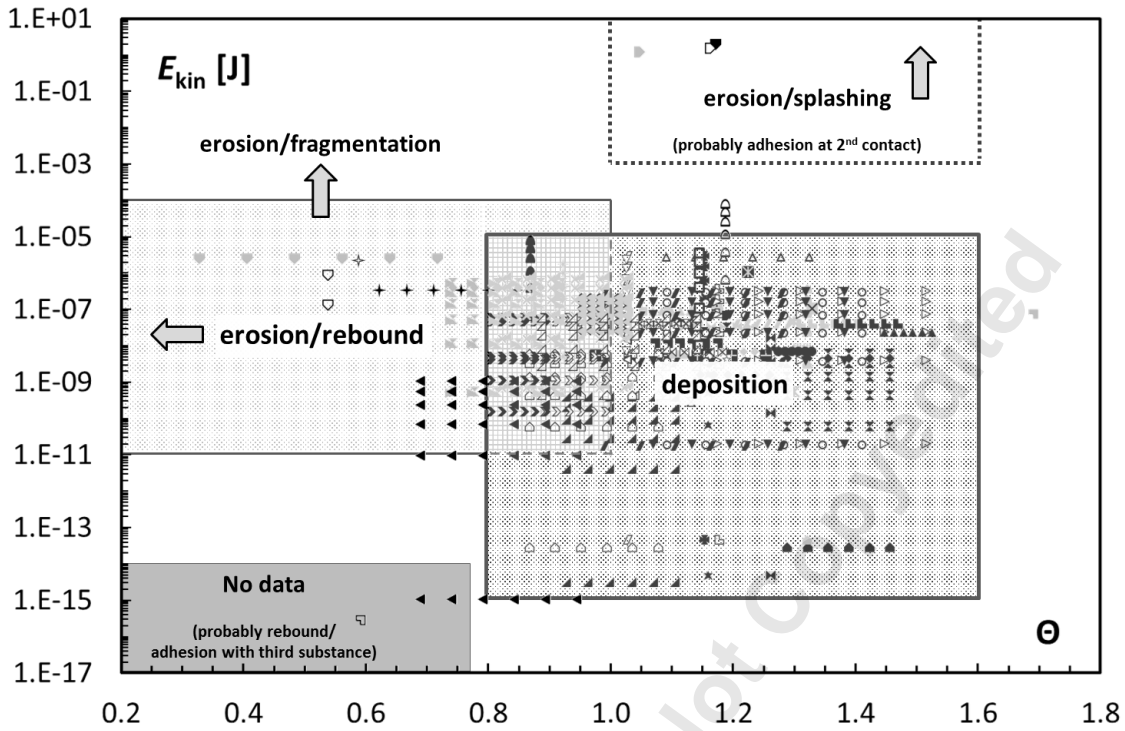

Figure_11_GTP-18-1525